Mixing state of carbonaceous aerosol in an urban environment: single particle characterization using the soot particle aerosol mass spectrometer (SP-AMS)

A. K. Y. Lee[1], M. D. Willis[1], R. M. Healy[2,3], T. B. Onasch[4], and J. P. D. Abbatt[1]

[1]Department of Chemistry, University of Toronto, Toronto, Canada
[2]Department of Chemistry and Environmental Research Institute, University College Cork, Cork, Ireland
[3]Southern Ontario Centre for Atmospheric Aerosol Research, University of Toronto, Toronto, Canada
[4]Aerodyne Research Inc., Billerica, Massachusetts, USA

Correspondence to: A. K. Y. Lee (klee@chem.utoronto.ca)

Abstract. Understanding the impact of atmospheric black carbon (BC)-containing particles on human health and radiative forcing requires knowledge of the mixing state of BC, including the characteristics of the materials with which it is internally mixed. In this study, we examine the mixing state of refractory BC (rBC) and other aerosol components in an urban environment (downtown Toronto) utilizing the Aerodyne soot particle aerosol mass spectrometer equipped with a light scattering module (LS-SP-AMS). k-means cluster analysis was used to classify single particle mass spectra into chemically distinct groups. One resultant particle class is dominated by rBC mass spectral signals (C_1^+ to C_5^+) while the organic signals fall into a few major particle classes identified as hydrocarbon-like organic aerosol (HOA), oxygenated organic aerosol (OOA), and cooking emission organic aerosol (COA). A gradual mixing is observed with small rBC particles only thinly coated by HOA ($\sim 28\%$ by mass on average), while over 90 % of the HOA-rich particles did not contain detectable amounts of rBC. Most of the particles classified into other inorganic and organic particle classes were not significantly associated with rBC. The single particle results also suggest that HOA and COA emitted from anthropogenic sources were likely major contributors to organic-rich particles with vacuum aerodynamic diameter (d_{va}) ranging from ~ 200 to $400\,\mathrm{nm}$. The similar temporal profiles and mass spectral features of the organic classes identified by cluster analysis and the factors from a positive matrix factorization (PMF) analysis of the ensemble aerosol data set validate the interpretation of the PMF results.

1 Introduction

Atmospheric black carbon (BC) particles play an important role in regional air quality and introduce large uncertainties into radiative forcing estimates of Earth's atmosphere (Bond et al., 2013). Fossil fuel combustion and biomass burning are the primary sources of ambient BC. Coatings on BC aerosol surfaces with varying morphology (e.g., partly coated and embedded) and thickness have been observed using electron microscopy (China et al., 2013, 2014). These coatings can be formed through condensation and coagulation of low-volatility materials co-emitted from combustion sources (e.g., unburned organics) and produced via photochemical processing during transport. Current research is evaluating whether particle coatings can significantly enhance the light absorption efficiency of ambient BC (Cappa et al., 2012; Jacobson 2001; Lack et al., 2012; Metcalf et al., 2013). Also, coating materials can modify the hygroscopicity and/or the cloud activation of BC particles, thus, affecting their atmospheric lifetime (McMeeking et al., 2011; Tritscher et al., 2011; Wang et al., 2010; Zhang et al., 2008). Improving our understanding of the mixing state of BC and the characteristics of its associated coatings is crucial to evaluate the fate and environmental impacts of ambient BC.

Real-time quantitative single particle detection (i.e., number concentrations, size distributions and chemical composition by mass in a single particle basis) is necessary to determine the mixing state of ambient particles. In particular, the single particle soot photometer (SP2, DMT, Inc.) has been developed to quantify refractory BC (rBC) using single particle incandescence signals (Baumgardner et al., 2004; Stephens et al., 2003). Combining both optical scattering and incandescence signals, the SP2 has been used to evaluate the degree of mixing (internal vs. external) and estimate the coating thickness of BC particles in both field and laboratory studies (e.g., Metcalf et al., 2013; Moteki and Kondo 2007; Schwarz et al., 2006; Shiraiwa et al., 2007, 2010). However, this instrument cannot characterize the chemical composition of the coating materials. Single particle mass spectrometry utilizing laser desorption/ionization methods such as the aerosol time-of-flight mass spectrometer (ATOFMS, TSI, Inc.) and particle analysis by laser mass spectrometry (PALMS) are powerful techniques, which provide rich size-resolved chemical information to examine the mixing state of both refractory (e.g., dust and BC) and non-refractory components in ambient particles (Pratt and Prather, 2012, and references therein). In particular, Prather and co-workers have undertaken a series of ATOFMS studies focused on vehicular and carbonaceous particle measurements (Cahill et al., 2012; Moffet and Prather, 2009; Shields et al., 2007, 2008; Sodeman et al., 2005; Toner et al., 2006, 2008). However, these single particle mass spectrometry techniques are number concentration-based methods and the associated pulsed laser desorption and ionization process makes particle mass quantification challenging (Pratt and Prather, 2012).

The Aerodyne aerosol mass spectrometer (AMS, Aerodyne Research Inc.) separates the particle vaporization and ionization steps to make quantification of particulate mass possible, with different versions of the AMS deployed to measure mass concentrations and mass-size distributions of non-refractory particulate matter (NR-PM) (e.g., Canagaratna et al., 2007; Drewnick et al., 2005; Jayne et al., 2000; Jimenez et al., 2009; Ng et al., 2010; Zhang et al., 2007). Specifically, the application of positive matrix factorization (PMF) analysis to AMS measurements has been developed to provide information on possible sources of organic aerosol and the extent of aerosol aging (Lanz et al., 2007; Ng et al., 2010; Ulbrich et al., 2009; Zhang et al., 2011). A few previous studies have demonstrated that a time-of-flight AMS in conjunction with a light scattering module (LS-ToF-AMS) can be used to characterize ambient particles on a single particle basis, which allows investigating the mixing state of NR-PM in ambient (Cross et al., 2009; Freutel et al., 2013; Liu et al., 2013). Different particle categorization approaches have been developed to analyze single particle data sets from the LS-ToF-AMS, including principle component analysis (Cross et al., 2009), k-means cluster analysis (Liu et al., 2013) and a classification algorithm based on comparison with reference mass spectra (Freutel et al.,

2013). Robinson et al. (2013) recently deployed the LS-ToF-AMS to determine the mixing state of laboratory-generated organic aerosol in a smog chamber. However, the LS-ToF-AMS is only able to detect non-refractory aerosol species that flash vaporize at $\sim 600\,^{\circ}\text{C}$.

The utility of the AMS was recently extended by development of the soot particle aerosol mass spectrometer (SP-AMS), which is able to quantify and characterize rBC (i.e., C_x fragmentation pattern and surface functionality) and NR-PM simultaneously (Cross et al., 2010, Onasch et al., 2012, Corbin et al., 2014). An infrared (IR) laser vaporizer has been incorporated into the standard high-resolution time-of-flight AMS (HR-ToF-AMS) to facilitate the detection of rBC components and associated coating materials. Incorporation of the light scattering module into the SP-AMS (LS-SP-AMS) allows the instrument to detect both rBC and NR-PM on a single particle basis. Thus, this technique enables the characterization of the mixing state of ambient carbonaceous particles, including rBC-containing, while simultaneously measuring the average size-resolved chemical compositions and mass loadings of the ensemble aerosol. However, the LS-ToF-AMS typically measures individual particles in ambient air with vacuum aerodynamic diameters (d_{va}) > 350 nm due to the lower sizing limit of the light scattering module (Cross et al., 2009; Freutel et al., 2013; Liu et al., 2013). It is crucial to investigate whether the LS-SP-AMS can detect fresh, less-coated rBC-containing particles derived from vehicle combustion, which are generally emitted at d_{va} well below the typical light scattering cutoff diameter (Massoli et al., 2012).

The primary objective of this study is to investigate the mixing state of ambient rBC-containing particles in an urban environment utilizing the single particle capabilities of the LS-SP-AMS. Cluster analysis using the k-means algorithm, which has been widely applied to analyze ATOFMS data, is performed to classify mass spectra from ambient single particles. Previous studies have shown that k-means clustering can classify ambient particle types measured by ATOFMS in good agreement with other clustering algorithms such as ART-2a and hierarchical clustering (Rebotier and Prather, 2007; Giorio et al., 2012). The clustering results are used to evaluate the mixing state of ambient particles measured in downtown Toronto and to validate the interpretation of factors from PMF analysis of simultaneously obtained LS-SP-AMS ensemble measurement data.

2   Experiment

2.1   Sampling location and instruments

An Aerodyne soot particle aerosol mass spectrometer (Aerodyne Research Inc.) equipped with a light scattering module (LS-SP-AMS) was deployed to measure both NR-PM (i.e., ammonium, nitrate, sulfate and organic) and rBC of

the ensemble aerosol and for single particles. A co-located scanning mobility particle sizer (SMPS; TSI Inc., model 3936L76) was used to measure ambient particle number concentrations and size distributions. The SMPS was set to scan every 4 min. The sheath-to-aerosol flow ratio was held at 10 : 1.

The urban sampling site was located at the St. George campus of the University of Toronto in downtown Toronto and the sampling period occurred during 18–22 September 2012 (from Tuesday evening to Saturday afternoon). The instruments were located on the third floor of the Lash Miller Chemical Laboratories (~ 10 m a.g.l.). The building is located near the intersection of St. George Street and Willcocks Street (Fig. S1 in the Supplement). St. George Street has a modest but steady traffic load during weekday rush hours. The aerosol sampling inlet was a 3/8 in. stainless steel tubing with the total flow rate of ~ 4 L min^{-1} and was pointing towards Willcocks Street, which has been blocked to traffic. There are a few catering facilities including a university canteen near the Lash Miller building and food carts along St. George Street.

2.2 Soot particle aerosol mass spectrometer

The working principle of the SP-AMS has been reported in detail previously (Onasch et al., 2012). In brief, the SP-AMS is a standard HR-ToF-AMS (DeCarlo et al., 2006) coupled with a diode-pumped Nd:YAG intracavity 1064 nm IR laser vaporizer (see Fig. 1). In the standard AMS configuration, a resistively heated tungsten vaporizer is operated at $\sim 600\,^\circ$C to vaporize the NR-PM (Canagaratna et al., 2007). The addition of the laser vaporizer expands the utility of the standard AMS to vaporize near-IR light absorbing aerosol particles, especially rBC. The rBC-containing particles are heated by absorbing IR energy to ~ 4000 K to facilitate their vaporization. The resulting gas phase species from either the laser or tungsten vaporizer are ionized with electron impact (EI) ionization (70 eV). The ions are then detected by a high-resolution time-of-flight mass spectrometer operated in V mode, which provides a lower mass resolving power (~ 2000) but a higher sensitivity compared to W mode (mass resolving power ~ 4000) (DeCarlo et al., 2006).

The SP-AMS was operated with two vaporizer configurations during sampling, laser-on and laser-off, to maximize the information obtained and to enable comparisons and correlations between the two different vaporizers. In particular, previous work has shown vaporizer-dependent differences in collection efficiencies and fragmentation patterns (Onasch et al., 2012; Willis et al., 2014). When the IR laser was off, the LS-SP-AMS was operated as a standard HR-ToF-AMS for measuring NR-PM as described above, whereas the instrument operated with the IR laser-on detected both rBC and NR-PM. An aerodynamically focused particle beam overlaps perpendicularly with the IR laser vaporizer before it hits the tungsten vaporizer and, hence, the NR-PM that is internally

mixed with rBC is vaporized by the IR laser (Onasch et al., 2012). A single slit chopper with ~ 2 % throughput was used in our LS-SP-AMS. In addition to the ensemble measurements (i.e., mass spectrum (MS) and particle time-of-flight (PToF) modes to measure bulk and size-resolved chemical composition, respectively), a light scattering module was integrated into the SP-AMS for detecting single particle mass spectra (LS mode, see Sect. 2.4 for details). The single particle data are particularly useful for determining the mixing state of ambient aerosol particles. Information on menu switching (90 s each) in the LS-SP-AMS is shown in Table 1.

2.3 Calibration and ensemble data analysis

Ammonium nitrate (NH_4NO_3) particles generated by a constant output atomizer (TSI Inc., Model 3076) were dried using a diffusion dryer and subsequently size-selected at 300 nm using a differential mobility analyzer (DMA, TSI Inc., Model 3081) for determining the ionization efficiency of the LS-SP-AMS when operated in the IR laser-off mode. Similarly, a water suspension of Regal Black (Regal 400R Pigment Black, Cabot Corp., a calibration standard recommended by Onasch et al., 2012) was atomized to generate standard rBC particles. Dried 300 nm Regal Black particles were used to determine the mass-based ionization efficiency of rBC, for calculation of the ionization efficiency relative to nitrate (RIE_{rBC}) (Onasch et al., 2012). The ensemble data were processed using the AMS data analysis software (Squirrel, version 1.51H, for unit mass resolution (UMR) data and Pika, version 1.10H, for high-resolution peak fitting, http://cires.colorado.edu/jimenez-group/ToFAMSResources/ToFSoftware/index.html) with the corrected air fragment column of the standard fragmentation table (Allan et al., 2004; DeCarlo et al., 2006).

Signals of rBC were quantified by the sum of carbon ion clusters (C_x^+) using high-resolution mass spectral data of up to m/z 120. The product of density and shape factor of the dried 300 nm Regal Black particles is ~ 0.8 g cm^{-3}, which is derived from the ratio of the vacuum aerodynamic diameter (d_{va}) measured by the PToF mode of the LS-SP-AMS to the mobility diameter (d_m) determined by the DMA (DeCarlo et al., 2004) as follows:

$$d_{va} = \rho \cdot S \cdot d_m / \rho_0, \tag{1}$$

where ρ and S are the density and Jayne shape factor of Regal Black particles, respectively, and ρ_0 is the unit density. The RIE_{rBC} determined in this study was 0.4, and the default RIE values of nitrate (1.1), sulfate (1.2), organics (1.4) and ammonium (4) were used (Jimenez et al., 2003). The average C_1^+ / C_3^+ ratio (0.61) obtained from Regal Black was used to correct the interference in C_1^+ from the non-refractory organics in ambient aerosol. The size distribution of rBC was calculated by adding an rBC column (C_1^+–C_5^+ fragments) to the fragmentation table in Squirrel as shown Table S1 in the Supplement. Note that Willis et al. (2014) reported that the

Table 1. Summary of menu switching in the LS-SP-AMS and single particle categorization.

Menu	1	2	3	4
IR laser mode	On	On	Off	Off
Data acquisition mode	MS, PToF	LS	MS, PToF	LS
Time intervals (s)	90	90	90	90
Total LS trigger events	–	113 120	–	112 441
"Noise" events	–	28 513	–	28 226
Particle LS trigger events	–	84 607	–	84 218
Coincidence	–	2190 (2.6 %)	–	2242 (2.7 %)
Prompt	–	35 001 (41.4 %)	–	28 322 (33.6 %)
Early	–	206 (0.2 %)	–	83 (0.1 %)
Delayed	–	702 (0.8 %)	–	340 (0.4 %)
Null	–	46 508 (55.0 %)	–	53 231 (63.2 %)
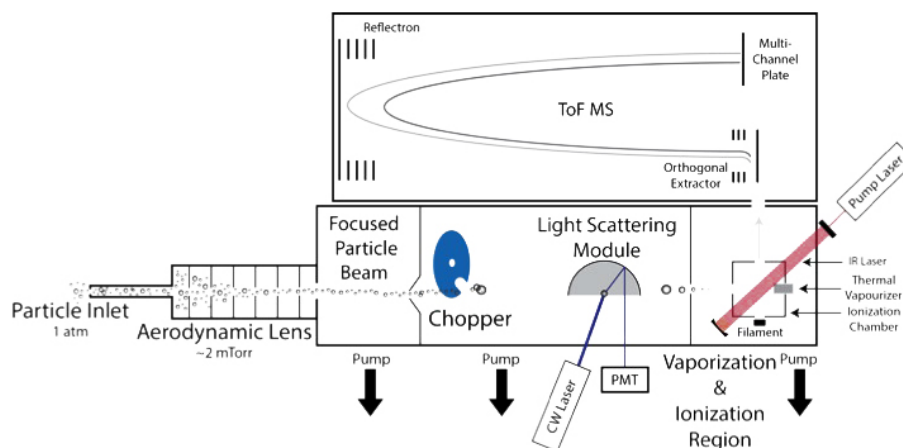
Figure 1. A simplified schematic of the SP-AMS equipped with a light scattering module (LS-SP-AMS) for ensemble measurements and single particle detection.

collection efficiency (CE) of bare Regal Black is about 0.6 for our instrument. Onasch et al. (2012) reported that the 3σ detection limit for rBC mass concentration measurements is $0.03 \, \mu g \, m^{-3}$ for 1 min collection.

2.4 Light scattering module for single particle detection

The design and working principles of the light scattering module have been previously described in detail (Cross et al., 2009; Freutel et al., 2013; Liu et al., 2013). Briefly, the light scattering module consists of a 50 mW diode-pumped 405 nm continuous-wave laser (CrystaLaser, LC BCL-050-405) that overlaps perpendicularly with the particle beam ~ 0.265 m downstream of the chopper and ~ 0.130 m upstream of the tungsten vaporizer as shown in Fig. 1. Note that the laser beam is not focused and diverges in order to ensure a complete overlap between the laser and particle beams (Cross et al., 2007). Scattered light from sampled particles is collected using an ellipsoidal mirror and detected with a pho-

tomultiplier tube (PMT). A light scattering signal can be obtained if a sampled particle is larger than the optical detection limit. The 50 % cutoff mobility diameter (d_m) (i.e., a diameter that represents a 50 % counting efficiency of a particle number when compared to a condensation particle counter) of our light scattering module determined using dry NH_4NO_3 particles is ~ 250 nm, which is approximately equal to a vacuum aerodynamic diameter (d_{va}) of ~ 340 nm (the density and shape factor of NH_4NO_3 particles are $1.72 \, g \, cm^{-3}$ and 0.8, respectively). Note that some ambient particles with lower particle densities may have a lower cutoff d_{va} than that determined for the dried NH_4NO_3 particles. For example, a hydrocarbon oil droplet (i.e., shape factor $= \sim 1$ and density $= \sim 1 \, g \, cm^{-3}$) likely has a light scattering cutoff in the range of 225–250 nm d_{va}.

2.5 Single particle categorization

Once a light scattering signal is detected, the computer is triggered to save the whole PToF trace, from which the sin-

gle particle mass spectrum is subsequently obtained. The PToF data (i.e., particle flight time between the running chopper and the light scattering laser or laser/tungsten vaporizer) can be used to calculate the d_{va} of all recorded single particles so that a size distribution of the entire single particle data set can be obtained. There are two major timing uncertainties for particle sizing measurement: (1) the initial time of the chopper cycle due to the slit width of the spinning chopper ($\sim 2\%$), and (2) the extra time required for vaporization, ionization and detection. Light scattering and single particle mass spectral measurements were processed using the AMS light scattering data processing software (Sparrow, 1.04E, http://cires.colorado.edu/jimenez-group/ToFAMSResources/ToFSoftware/index.html), which is designed for analyzing mass spectra with UMR only.

Weak scattering trigger events (i.e., a total scattering signal of less than 0.2 V or a signal-to-noise ratio less than 5) were classified as "noise" events and were not included in the subsequent particle categorization. For particles that gave a sufficiently strong LS trigger event (i.e., those are not classified as "noise") and a total number of ions ≥ 6 in their mass spectra (calculated by integrating the ion signals in the single particle mass spectrum), they were categorized as either "prompt", "early" or "delayed" particle types based on their PToF information (see supplementary information for information on setting the LS signal and total number of ion thresholds). When the PToF recorded by the light scattering signal (LS$_{PToF}$) can accurately predict the particle arrival time to the mass spectrometer (MS$_{PToF}$) the particle is categorized as prompt. The Gaussian fit of the difference between LS$_{PToF}$ and MS$_{PToF}$ (i.e., LS$_{PToF}$ − MS$_{PToF}$) was used to define the prompt particle boundaries (i.e., particles falling outside the Gaussian fit boundaries (3σ) were assigned as either "early" or "delayed" particle types) (Fig. S2). The delayed particle type can be due to the phenomenon of particle bounce upon impact with the thermal vaporizer surface (i.e., delayed vaporization) (Cross et al., 2009) but the physical meaning of early particle type remains unclear.

The calculation of total ion signals of an individual particle was modified in the standard software. Instead of using the default output from the fragmentation table, the total number of ions was calculated as the sum of all ion signals except m/z 14 (N$^+$), 15 (NH$^+$), 16 (NH$_2^+$), 17 (NH$_3^+$), 18 (H$_2$O$^+$), 28 (N$_2^+$), 32 (O$_2^+$) and 39 (K$^+$) due to either the strong interferences from air and instrument background (i.e., surface ionization on the tungsten vaporizer for K$^+$) or the noisy baseline of ammonium fragment ions. Multiple scattering signals observed in a trigger event and weak total ion signal (< 6 ions) were recognized as "coincidence" and "null" particle types, respectively. A summary of the particle categorization in different LS-SP-AMS modes is presented in Table 1. The size distributions of prompt particles in terms of light scattering signal intensity and total number of ions in an individual particle spectrum are shown in Fig. S3. It is ap-

parent that the particle categorization procedure effectively separates the prompt particles from the full collected single particle data set.

2.6 Cluster analysis of single particle data

Cluster analysis was performed to investigate the mixing state of prompt particles based on the k-means algorithm in IGOR Pro (WaveMetrics Inc., version 6.2.2.2). Including other particle types with a lower confidence on their PToF d_{va} (i.e., early and delayed) to the cluster analysis would not affect the major observations, as they contributed only $\sim 1\%$ of the particle LS trigger events (Table 1). k-means cluster analysis has been extensively applied to analyze single particle data measured from the TSI ATOFMS (Rebotier and Prather, 2007; Friedman et al., 2009; Giorio et al., 2012; Gross et al., 2010; Healy et al., 2010, 2013; Pagels et al., 2013) and more recently a standard HR-ToF-AMS with a light scattering module (Liu et al., 2013). It is worth noting that k-means clustering can classify ambient particles measured by ATOFMS into particle types that are highly consistent with other clustering algorithms such as ART-2a and hierarchical clustering (Rebotier and Prather, 2007; Giorio et al., 2012). Similar to the calculation of total ion signals in a single particle mass spectrum, m/z 14, 15, 16, 17, 18, 28, 32 and 39 were excluded in the cluster analysis. All single particle mass spectra were normalized by their total ion signal, and solutions with up to 25 clusters were tested. Euclidian distance (the square root of the sum of the squares of the differences between corresponding values) was used to evaluate the total distance between the cluster centers and each single particle. In general, increasing the number of clusters can better represent the data set mathematically (i.e., reduce the total distance) as shown in Fig. S4. However, a very large number of clusters compromises the physical meaning of each cluster.

A cluster analysis panel (CAP) recently developed by our group was used to perform the built-in k-means clustering algorithm in IGOR Pro. The following information for each cluster can be directly generated by CAP: (1) number of particles, (2) normalized ion-weighted average unit mass resolution mass spectrum, (3) normalized histogram of the frequency of occurrence for each m/z ion signal for each single particle, and (4) average, time- and size-resolved chemical composition (nitrate, sulfate, organics and rBC) in terms of ion counts. Note that the CAP can also merge multiple clusters into a single particle class if they have similar mass spectral features and size distributions, whereas other clusters remain unchanged. To avoid generating negative ion signals from the default fragmentation table in Sparrow, a simplified version of the fragmentation table was applied for calculating the chemical composition as shown in Table S2.

3 Results and discussion

This section is divided into two main parts. The first part (Sect. 3.1–3.3) presents the observations from SP-AMS ensemble aerosol measurements and PMF analysis of the organic components. The second part (Sect. 3.4–3.9) focuses on identification of particle types and characterizing the mixing state of carbonaceous aerosols based on cluster analysis of LS-SP-AMS single particle measurements. Note that the ensemble measurements detect particles with d_{va} starting from ~ 50 nm and up to ~ 1 μm, whereas the single particle measurements only detect particles greater than 200 nm d_{va} (the LS cutoff diameter for different particle types will the discussed in Sect. 3.4).

3.1 Overview of ensemble measurements

Figure 2a shows the time series of NR-PM, measured by the IR laser-off mode (i.e., the standard HR-ToF-AMS configuration), and rBC, measured in IR laser-on mode, of the whole sampling period in downtown Toronto. In general, organics dominated the particulate mass, whereas rBC contributed 4–9 % of the average particle mass, assuming the CE for ambient rBC varies between 0.6 and 1 (i.e., CE range for bare and heavily coated Regal Black particles, respectively) (Willis et al., 2014) and the CE for all NR-PM evaporated from the tungsten vaporizer varies between 0.5 and 1 depending on chemical composition (Middlebrook et al., 2012) (see Fig. S5 and calculation details based on single particle data in the Supplement). Willis et al. (2014) reported that the particle beam width (i.e., a primary parameter that governs the CE of rBC in SP-AMS) of ambient rBC particles measured at the same location of downtown Toronto is similar to that of heavily coated Regal Black particles generated in the laboratory. The total particle mass loading measured by the LS-SP-AMS is similar to that inferred from a simultaneous measurement using a scanning mobility particle sizer (SMPS, TSI Inc.) (slope ~ 1.02, $R^2 = 0.76$), suggesting that the estimated CEs for NR-PM, vaporized from the heated tungsten vaporizer, and rBC, vaporized from the laser vaporizer, are within reasonable ranges (see Fig. S5).

The average mass spectrum of rBC was dominated by carbon ion clusters from C_1^+ to C_5^+ (~ 95 %), with the strongest rBC signal at C_3^+ (Fig. 2b). These spectral characteristics are similar to previous SP-AMS measurements (Massoli et al., 2012; Onasch et al., 2012) and the calibration standard used in the current study (Regal Black, see insert in Fig. 2b). Fullerene-type rBC spectral features (i.e., C_x^+ fragments with carbon number > 32) cannot be evaluated because their C_x^+ peaks are out of the m/z range (up to ~ 300) investigated in this study. Onasch et al. (2012) observed carbon cluster ions of up to C_{82}^+ in laboratory-generated ethylene flame soot particles and detected C_{32}^+–C_{70}^+, which accounted for about 4 % of the total rBC signals at an urban roadside environment. Furthermore, Dallmann et al. (2014) have demonstrated the

capability of the SP-AMS to detect trace metals such as zinc in on-road gasoline and diesel vehicles emissions. However, no trace metals were clearly observed in this study.

Figure 2c displays the average ensemble size distributions (PToF d_{va}) of NR-PM and rBC. Secondary inorganic species, nitrate and sulfate, peaked at ~ 300–400 nm with much less contribution to the mass of smaller size particles. In contrast, the rBC signals peaked at ~ 100 nm. Since ambient rBC is only emitted from primary sources, this suggests that a significant portion of the sampled rBC was freshly emitted or only slightly aged particles. This is consistent with the fact that vehicle emissions are a major local source of rBC in the downtown area of Toronto. Organic species covered a wide range of particle sizes, indicating that they may be internally mixed with rBC and inorganic species. The organic fragment at m/z 44 (Org44, CO_2^+) that can be used as a tracer of oxygenated organic aerosol (OOA) (e.g., organic acids) exhibited a bimodal distribution with the larger particle mode comparable to sulfate and nitrate (Fig. 2c). Nevertheless, additional information such as single particle characterization is required to confirm the mixing state of ambient particles. The average O / C and H / C ratios of total organics obtained from elemental analysis of high-resolution mass spectral data are 0.28 (ranging from 0.05 to 0.57) and 1.65 (ranging from 1.47 to 1.82), respectively (see the Van Krevelen diagram in Fig. S6). The relatively low fraction of oxygenated organic aerosol indicates that the sampling site was strongly influenced by local anthropogenic sources, such as vehicle- and cooking-related emissions, matching well with the site characteristics (see Sect. 2.1).

3.2 PMF analysis of ensemble measurements

PMF has been widely applied to analyze ambient AMS data sets to identify the potential sources of organic aerosol (Ulbrich et al., 2009; Zhang et al., 2011). PMF analysis separates the total organics measured in this study (Fig. 3a–c) into factors that have been commonly observed in AMS measurements: hydrocarbon-like organic aerosol (HOA), cooking emission organic aerosol (COA), and OOA (Zhang et al., 2011, and references therein). In brief, the HOA spectrum exhibits fragmentation patterns associated with hydrocarbon structures (e.g., m/z 57 ($C_4H_9^+$) and 69 ($C_5H_9^+$)), and is comparable to those of gasoline/diesel vehicle exhaust and lubricating oil (Canagaratna et al., 2004; Massoli et al., 2012; Mohr et al., 2009). The COA and HOA spectra are similar to each other; however, the COA factor tends to have a higher m/z 55 / 57 ratio (Allan et al., 2010; Mohr et al., 2009, 2012). Lastly, the OOA spectrum is composed of a relatively high fraction of m/z 44 (CO_2^+), indicating that the OOA material has a higher photochemical age (Jimenez et al., 2009; Ng et al., 2010). The O / C and H / C ratios of the laser-off-mode PMF factors and their coordinates in the Van Krevelen diagram are shown in Figs. 3a–c and S6, respectively.
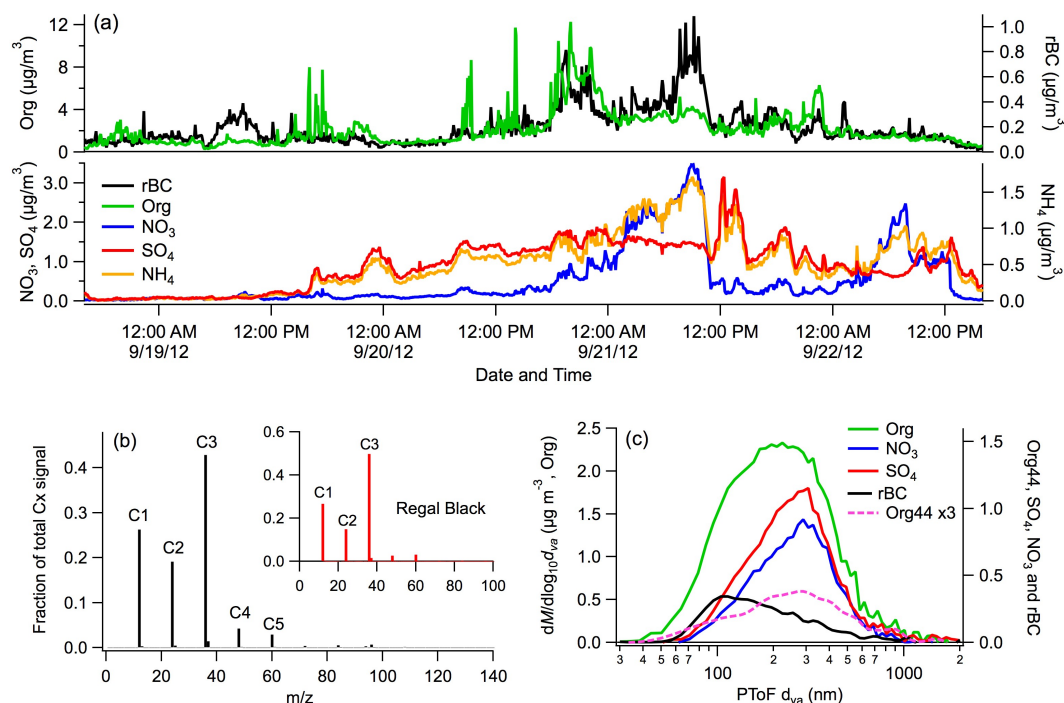
Figure 2. Summary of ensemble measurements. **(a)** Time series (local time) of laser-off (Org, NO_3, SO_4, NH_4) and laser-on (rBC) aerosol compositions. **(b)** The average mass spectrum of laser-on ambient rBC and Regal Black (insert). **(c)** Average size distributions of laser-off (Org, NO_3, SO_4, Org44) and laser-on (rBC) aerosol compositions. Org44 represents the organic signal at m/z 44 (e.g., CO_2^+).

Figure 4 shows the time series of the three-factor PMF solution obtained with the IR laser-off. Significant contributions of HOA and COA to the total organic mass (average ± standard deviation = 52 % ± 20 %) indicate that the sampling site was strongly influenced by anthropogenic emissions (Fig. S7). In particular, the temporal variations in rBC and the laser-off HOA factor showed a significant correlation (Fig. 4a), demonstrating that the HOA was primarily emitted from combustion sources such as engine exhaust. The substantial COA mass loading is consistent with the fact that many catering facilities are close to the sampling site (Fig. 4b). The strong diurnal cycle of the COA factor was likely due to the active cooking activities from noontime to nighttime every day. The OOA factor represents the ambient level of oxygenated organic aerosol that originated from secondary sources and/or was produced by photochemical aging (e.g., transported/regional emissions from outside the city) (Fig. 4c). Similar PMF results were obtained for the IR laser-on measurements (excluding rBC signals in the PMF analysis) and are shown in Figs. S8 and S9. Including the rBC signals only slightly modified the PMF results of the laser-on measurements as displayed in Figs. 3d–f and S8. Based on the PMF analysis, the rBC mass in HOA, COA and OOA factors accounted for about 51 % (±20 %), 9 % (±11 %) and 40 % (±18 %), respectively, of the total rBC mass loading, on average (± standard deviation). The temporal variations of the rBC mass fractions contributed by each factor are shown

in Fig. 3g. The comparison between PMF and single particle cluster analysis (Fig. 4, line vs. filled area) will be discussed in Sect. 3.9.

3.3 Comparison of laser-on and off ensemble measurements

The IR laser-on mode exhibited a higher sensitivity to all NR-PM components than the IR laser-off mode by ∼ 10–20 %, depending on the chemical species (Fig. S10). There are two likely explanations for these observations, both of which may account for all or part of the discrepancies. (1) The observed discrepancies may be due to different CE issues for the two vaporizers (i.e., incomplete particle-laser beam overlap for laser vaporizer (Willis et al., 2014) and particle bounce issues for tungsten vaporizers, Matthew et al., 2008). For example, the instrument operated in the laser-off mode might have a lower CE for rBC-containing particles due to particles bouncing off the tungsten vaporizer, an effect which would depend on the coating thickness, morphology and properties. As a result, some NR-PM components that are internally mixed with rBC may not be detected in the laser-off mode. In particular, it is well known that solid/semi-solid particles have a more pronounced bouncing effect than liquid particles (Docherty et al., 2013; Matthew et al., 2008). (2) Particle vaporization by the IR laser and the tungsten vaporizer do not occur at exactly the same location inside the ion chamber,

possibly resulting in different ionization rates and ion transmission efficiencies (i.e., from the ion chamber to the ion focusing optics) between the two operational modes. This difference may also be a reason for the observed enhancements in the RIE of NR-PM evaporated from rBC particles.

Although the main driver of the observed sensitivity enhancement remains unclear, a larger difference between the two modes would imply that a higher mass fraction of a particular aerosol component coexists with rBC, because rBC-containing ambient particles are evaporated by the IR laser before they can reach the tungsten surface. Compared to the standard AMS measurements, in the laser-on mode the HOA, COA and OOA mass loadings are higher by about 40, 10, and 23 %, respectively (Fig. S11a–c). Figure S11d explicitly demonstrates that the percentage difference of each PMF factor between the laser-on and off operational modes is positively correlated with the mass fraction of the rBC signal in each factor (mass fraction of rBC in laser-on HOA = 0.15, COA = 0.02, and OOA = 0.06). This is indirect evidence that a larger fraction of HOA material was internally mixed with rBC compared to the COA and OOA components. Furthermore, we note that HOA and COA (oil-like droplets) dominated the organic aerosol mass and, as indicated earlier (see Sect. 3.1, and Fig. S5 and description in the Supplement), these chemical components have CEs from the heated tungsten vaporizer close to unity, which would minimize the effects of the first argument. Therefore, the second argument is likely more appropriate to explain our observations for organic aerosol. For inorganic species, the enhancement of NH_4^+ mass between the two operational modes is smaller than those observed in the cases of NO_3^- and SO_4^{2-} (Fig. S10). The reason of this observation is unclear but one of the possibilities is that some refractory nitrate and sulfate (e.g., Na_2SO_4) coexisted with rBC. The direct measurements of mixing state from the single particle data will be discussed in the following sections.

3.4 Overview of single particle data set

The single particle statistics of the LS measurements are summarized in Table 1. The IR laser-on and off modes had 113 120 and 112 441 total LS trigger events, respectively, and 75 % of them in both laser-on and laser-off modes were recognized as particle LS trigger events. Approximately 41 % (35 001) and 34 % (28 322) of the particle LS trigger events were categorized as prompt particles in the laser-on and off modes, respectively. Figure 5 shows the prompt single particle results for laser-on and off modes, and the difference, as a function of the measured particle sizes (d_{va} nm). A higher fraction of prompt particles observed in the IR laser-on mode could be due to (1) the extra ions generated from rBC, (2) the different CE for laser and tungsten vaporizers especially for inorganic particles in the accumulation mode (see Fig. S5 and description in supplementary information), and (3) a higher mass spectral sensitivity (i.e., a higher RIE of NR-PM) in the

laser-on mode as described in Sect. 3.3. Cross et al. (2009) and Liu et al. (2013) reported that null particles accounted for ~ 50 % of the particle LS trigger events, which is somewhat lower than those determined in this study (Table 1). This may arise from the fact that all ammonium fragments (m/z 14, 15, 16) were excluded in our calculation of total ion signals in the particle categorization procedure. It is also worth noting that Cross et al. (2009) deployed a more sensitive compact ToF-AMS (CToF-AMS) in their measurements.

Figure 6 shows some representative examples of single particle mass spectra of rBC-containing particles. Using the ensemble spectrum of rBC as a reference (Fig. 2b), it is clear that ambient rBC can exist as nearly externally mixed (Fig. 6a) or can be associated with various types of coating materials such as HOA (Fig. 6b), OOA and inorganics (Fig. 6c). Figure 7 shows the chemically speciated size distributions of all prompt particles. A comparison between the single particle size distributions (Fig. 7) and the ensemble PToF data (Fig. 2c) illustrates the effect of the light scattering cutoff, showing that a significant portion of small particles cannot be detected in the LS measurements. A light scattering cutoff d_{va} of ambient nitrate and sulfate match well with that calibrated by the dried NH_4NO_3 particles, whereas ambient organic particles that are mainly composed of HOA and COA materials (see Sect. 3.5) have a cutoff d_{va} similar to that estimated for spherical hydrocarbon oil droplets (~ 250 nm, the pink dashed line in Figs. 5 and 7). Furthermore, the LS mode can detect rBC-containing particles and the associated coating materials down to ~ 100 nm d_{va}. This is because ambient BC/soot agglomerates can have low effective particle densities due to their fractal morphologies (China et al., 2013, 2014; Slowik et al., 2004). In other words, the ambient rBC particles that have small d_{va} can be physically large enough to be detected by the light scattering module (see Eq. 1) and can produce a sufficient signal for mass spectrometric detection.

The differences in overall and chemically speciated size distributions of ion signals between the laser-on and off modes are shown in Figs. 5 and 7c, respectively. Accumulation-mode particles peaked at ~ 400 nm d_{va} (mainly composed of secondary aerosol components such as nitrate, sulfate and oxygenated organic species) and exhibited the largest differences between the two operational modes. Organics with mid-range d_{va} (i.e., peak at ~ 300 nm) show a relatively small difference compared to accumulation-mode organics, suggesting that those organic particles are likely less sensitive to the types of particle vaporization (i.e., no rBC core). Note that those mid-range d_{va} organic particles are dominated by HOA and COA materials with a relatively small mass fraction of rBC (see Sect. 3.5). Similar observations are also obtained from particle number size distributions as shown in Fig. S12a. The laser-on-to-laser-off ratios in terms of total ion signals and particle number are biased higher in the large and small particle size ranges. The former is suggestive of potential bounce effects
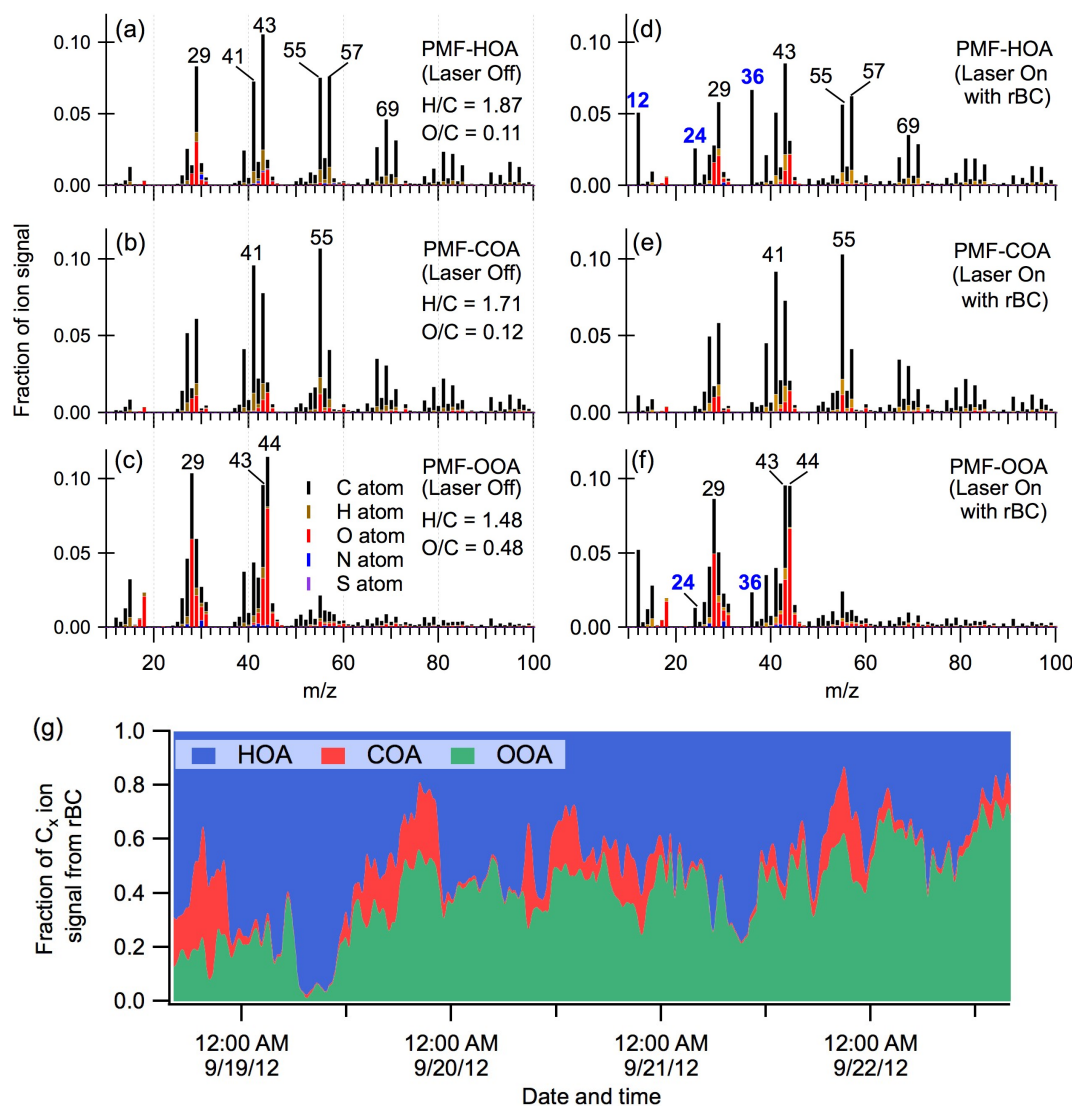
Figure 3. Normalized mass spectra of PMF factors from laser-off (**a–c**) and laser-on with rBC signals (**d–f**) mode measurements: (**a, d**) HOA factor, (**b, e**) COA factor, (**c, f**) OOA factor. (**g**) Mass fraction contribution of total C_x signal from each laser-on-mode PMF factor (**d–f**).

on the tungsten vaporizer and/or better ion transmission efficiency in the laser-on mode as discussed in Sect. 3.3; the latter, for particles smaller than 200 nm, is likely due to rBC particles dominating the ion signals (Fig. S12b).

3.5 Cluster analysis of single particle data sets

The k-means clustering algorithm was used to separately classify all the prompt particle mass spectra into chemically distinct groups for both laser-on and laser-off data sets. The overall cluster analysis results for NR-PM are similar for both the IR laser-on and off data sets, with the primary exception being an additional particle class, rBC, obtained from the laser-on-mode single particle data. The major NR-PM particle classes obtained via independent cluster analysis for both data sets included nitrate, sulfate, HOA, COA, and two types

of OOA (Fig. 8). These particle classes represented similar particle number fractions and time series, and differed only slightly in average mass spectra (not shown).

To demonstrate the capability of the LS-SP-AMS to investigate the mixing state of ambient aerosol particles, the 12-cluster solution from the laser-on mode measurements is presented here. The number of particles and the ion fractions of nitrate, sulfate, organics and rBC in each cluster are shown in Fig. S13. Increasing the number of clusters from 12 to 25 only gradually reduces the total Euclidian distance between the cluster centers and each single particle mass spectrum (Fig. S4), and does not generate any new particles classes with significant physical meaning (i.e., determined by cluster re-combinations as discussed in the next paragraph). Note that an rBC-rich particle class (see Sect. 3.5.2) can be clearly
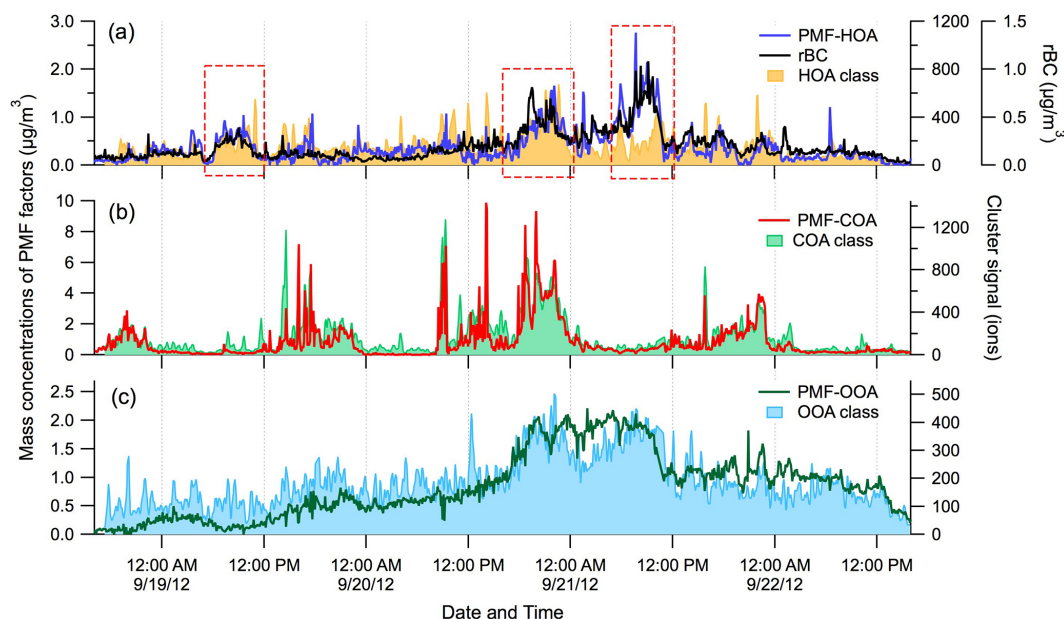
Figure 4. Time series (local time) profiles of rBC and PMF factors of organic components (from laser-off-mode MS measurements) and different organic clusters (from laser-on-mode LS measurements). The red rectangles indicate three major rBC and HOA peaks throughout the sampling period.
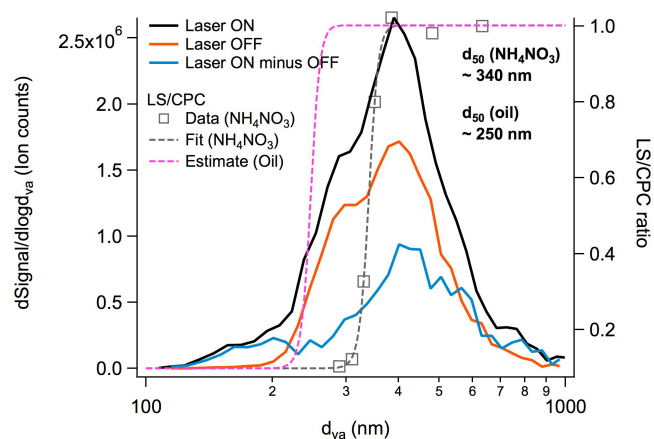
Figure 5. Size distributions of total ion counts from the ambient single particle measurements (black: laser-on mode, orange: laser-off mode, blue: difference between laser-on and laser-off modes). The grey square (data) and grey dashed line (fitting) represent the counting efficiency (the ratio of light scattering counts and condensation particle counter signals (LS/CPC), left axis) of the light scattering module for ammonium nitrate particles. The pink dashed line indicates an estimated light scattering cutoff d_{va} for spherical hydrocarbon oil droplets (i.e., shape factor = 1 and density = 1 g cm^{-3}).

Figure 6. Examples of single particle mass spectra of rBC-containing particles in ambient air: **(a)** black carbon, **(b)** black carbon internally mixed with HOA, and **(c)** black carbon internally mixed with OOA and sulfate. Particles **(a)** and **(b)** are sorted into the rBC cluster, and particle **(c)** is classified into the OOA cluster 2 identified in this study (see Sect. 3.5).

identified starting from the nine-cluster solution (up to 25-cluster solution). However, for the 11-cluster solution, the rBC-rich particle class cannot be separated from OOA in the accumulation mode (i.e., d_{va} peak at ∼ 400 nm). Therefore,

the 12-cluster solution is considered as the optimal clustering solution.

By comparing the mass spectra, time series, and size distributions of the 12 clusters, it is clear that some clusters must be re-combined into a single particle class to provide physi-
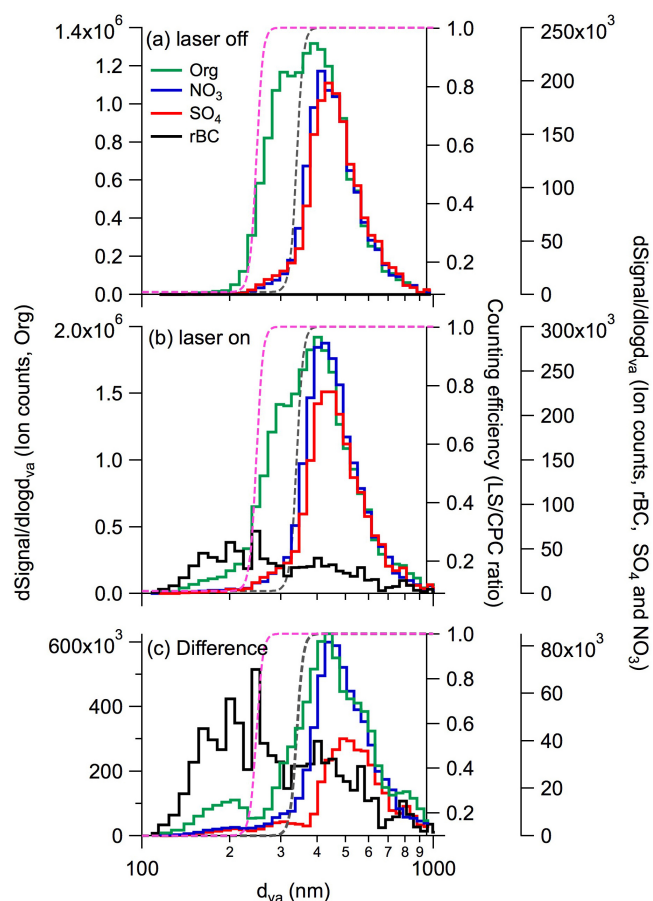
Figure 7. Integrated size distributions of nitrate, sulfate, organics and rBC from the single particle ion signal measurements with IR laser-off **(a)** and on **(b)**. **(c)** Differences between laser-on and off modes (i.e., laser-on minus laser-off data). The grey dashed line represents the counting efficiency (LS/CPC) of the light scattering module for ammonium nitrate particles. The pink dashed line indicates an estimated light scattering cutoff d_{va} for spherical hydrocarbon oil droplets.

cally meaningful results. For example, four preliminary clusters obtained from the k-means clustering (clusters 1, 6, 8 and 11 in Fig. S13) are rich in nitrate signatures with similar temporal variations and/or size distributions (Fig. S14) and, hence, they were merged to produce a single nitrate-rich class. Merging preliminary clusters into a single final particle class has been widely applied to cluster analysis of ATOFMS data (e.g., Healy et al., 2013). A tracer for rBC (C_3^+ at m/z 36) is used to examine the mixing state of ambient rBC. The potential isobaric interference from HCl^+ was evaluated based on the cluster analysis of the IR laser-off data set (Table 2, see discussion below).

3.5.1 Inorganic classes

Figure 8 summarizes the UMR spectra, mass spectral histograms and size distributions of the seven final particle classes. Figure 8a shows a nitrate-rich class that consists of significant ion signals at m/z 30 (NO^+) and m/z 46 (NO_2^+) with comparable intensities, and a sulfate-rich class with a mass spectrum dominated by m/z 48 (SO^+), 64 (SO_2^+), 80 (SO_3^+), 81 (HSO_3^+) and 98 ($H_2SO_4^+$). These inorganic classes have narrow size distributions and peak at ~ 400 nm (Fig. 8p, q), which is consistent with the PToF ensemble data. A significant fraction of the particles in these two classes are internally mixed with a substantial amount of organic material (see Sect. 3.6 for the discussion of mixing state of secondary species in an accumulation mode particle). The mass spectra of these organics are similar to the OOA class 1 identified in this work (i.e., strong signals at m/z 29 and 43; Fig. 8f). In particular, approximately 60–70 % of the nitrate- and sulfate-rich particles exhibit organic signals at m/z 43 (Fig. 8h, i). Furthermore, the tracer of rBC (C_3^+ at m/z 36) indicates that rBC has only a minor contribution to the nitrate- and sulfate-rich particles (i.e., a similar percentage of particles contributed to m/z 36 between laser-on and off modes ($< 2\%$) in these clusters) as shown in Table 2.

3.5.2 HOA and rBC classes

A cluster with mass spectral fragmentation patterns for hydrocarbons (i.e., $C_xH_y^+$ ions) is assigned as a HOA-rich class (Fig. 8c). Most of the HOA-rich particles do not contain any inorganic species (Fig. 8c, j). About 6 % of the HOA-rich particles were composed of a detectable signal at m/z 36 that originates from rBC (Table 2), and the mass contribution of rBC to this cluster was about 3 % on average ($RIE_{org} = 1.4$ and $RIE_{rBC} = 0.4$). Instead, the cluster analysis yields a separate rBC class without substantial organic coating (Fig. 8d). Although the mass fraction contribution of organics to this particle type is only 0.28, ~ 60–80% of the particles consist of detectable organic signals at m/z 41, 43, 55, and 57 (Fig. 8k). The rBC-rich class has a C_1^+ / C_3^+ ratio of about 0.53, which is slightly smaller than the ratio obtained from the calibration standard (Regal Black). The mass spectral character of the organic coating is similar to the spectrum of PMF-HOA in general, but with a slightly higher fraction of m/z 44 and lower fraction of m/z 55 and 57 compared to the HOA-rich class (insert of Fig. 8d). We emphasize that while PMF analysis showed that rBC and HOA materials likely have the same emission sources, this approach does not provide direct information about the ambient particle mixing state. In contrast, the cluster analysis clearly suggests that two major types of particles, which have different size distributions (Fig. 8r, s) and extents of internal mixing of HOA and rBC (see Sect. 3.7), contributed to the PMF-HOA factor.

3.5.3 COA and OOA classes

The mass spectrum of a COA class is shown in Fig. 8e. The COA cluster covers a range of particles with d_{va} peaking at ~ 300 nm (Fig. 8t). Similar to the PMF-COA factor, the COA
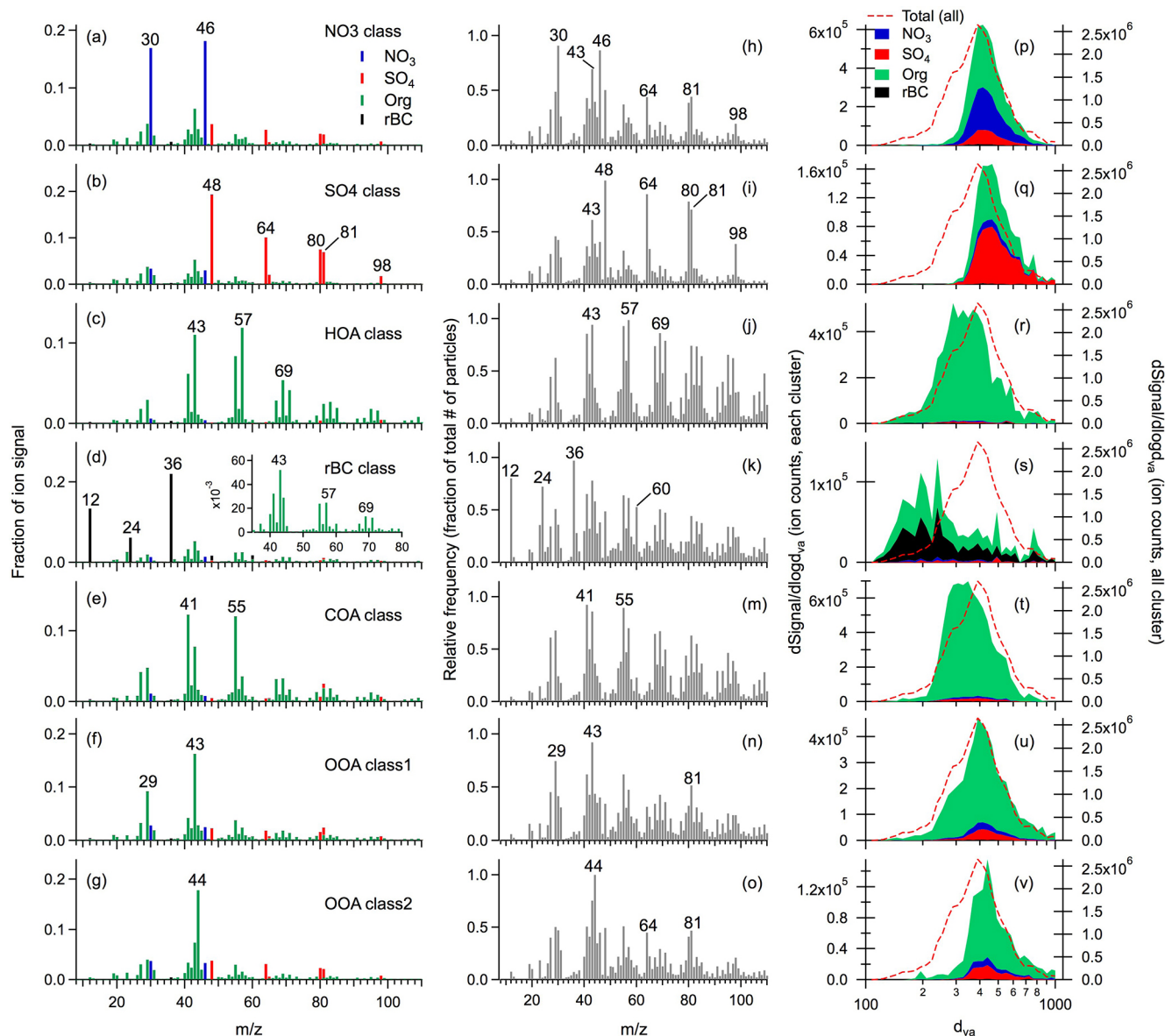
Figure 8. Normalized mass spectra (left column), normalized histograms displaying the relative frequency of each m/z (middle column), and size distributions (right column) of different particle classes identified from k-means clustering of LS-SP-AMS single particle data set (laser-on): (**a, h, p**) NO_3 class, (**b, i, q**) SO_4 class, (**c, j, r**) HOA class, (**d, k, s**) rBC class, (**e, m, t**) COA class, (**f, n, u**) OOA class 1 – less oxygenated, (**g, o, v**) OOA class 2 – more oxygenated. The insert in (**d**) shows the organic mass spectrum associated with rBC-rich particle class.

class is dominated by fragments at m/z 41 and m/z 55 with a relatively high m/z 55 / 57 ratio compared to the HOA. Two OOA classes were also identified (Fig. 8f, g). These particle types likely represent aged organic aerosol components because a large fraction of the particles (> 50 %) are associated with secondary nitrate and sulfate (see Sect. 3.6). While OOA class 1 represents the less oxygenated organics (i.e., strong signal from less oxygenated fragments such as CHO^+ at m/z 29 and $C_2H_3O^+$ at m/z 43), OOA class 2 has the distinct spectral feature of highly oxygenated organics pro-

duced via photochemical aging (i.e., intense signal at m/z 44 (CO_2^+) from organic acids). Both OOA classes have size distributions similar to the inorganic classes (see Sect. 3.6 for the discussion of mixing state of secondary species in an accumulation mode particle). The major exception is that the OOA class 1 has another peak with a smaller mean particle diameter, suggesting that this particle type may consist of ambient particles with a different degree of aging (e.g., fewer condensed materials such as inorganic species on the smaller particles). The majority of the particles in the COA and OOA

Table 2. Summary of the rBC contribution to each cluster.

Cluster type	% of particles with measurable m/z 36[a] signal (no. of particles)			Mass fraction of rBC (IR laser on)[b]
	Laser on	Laser off	Difference (laser on minus off)	
NO$_3$	11.4 % (1063)	10.2 % (652)	1.2 %	0.035
SO$_4$	4.4 % (130)	2.8 % (67)	1.6 %	0.019
HOA	8.4 % (347)	2.0 % (65)	6.4 %	0.024
rBC	97.1 % (867)	n/a	n/a	0.722
COA	6.5 % (548)	2.9 % (205)	3.6 %	0.020
OOA 1	8.2 % (587)	4.1 % (291)	4.1 %	0.027
OOA 2	7.4 % (153)	3.9 % (80)	3.5 %	0.028

[a] Any signal larger than zero, IR laser-on mode: m/z 36 = C$_3^+$ and HCl$^+$, IR laser-off mode: m/z 36 = HCl$^+$ only; n/a = not applicable. [b] The fragmentation table shown in TableS2 was used for quantification of rBC.

classes (96–97 %) were not associated with rBC signals (Table 2).

3.6 Mixing of secondary species in accumulation mode particles ($d_{va} \sim 400$ nm)

Although seven particle classes with their distinct mass spectral features are identified based on cluster analysis, atmospheric aerosol particles are likely internal mixtures with varying relative compositions of the different chemical components. As shown in Sect. 3.5, a few particle classes dominated by secondary species, including nitrate, sulfate, and OOA, are predominately measured by size to be in the accumulation mode (Fig. 8). To understand the mixing state of these secondary components, the relative mass contributions of nitrate, sulfate and organics (i.e., OOA) in each particle type are examined using ternary diagrams as shown in Fig. 9. The input parameters of ternary diagrams are converted from ion counts to mass-based data using default RIE of nitrate, sulfate and organics (see Sect. 2.3). Overall, all these particle types are internal mixtures of nitrate, sulfate and organics to different degrees. Most of the classified as nitrate-rich are composed of nitrate and organics, though some particles have significant sulfate content (up to ~ 50 wt % of these secondary species) (Fig. 9a). Figure 9b shows that the sulfate-rich class is dominated by internal mixtures of sulfate and organics with relatively low nitrate mass (up to ~ 30 wt %). OOA1 and OOA2 classes are dominated by organic-rich particles with a variable degree of internal mixing with sulfate and nitrate (up to ~ 40 and ~ 30 wt %, respectively) (Fig. 9c). In contrast, a very low degree of internal mixing of inorganic components with COA, HOA and rBC classes are observed (see ternary diagrams shown in Fig. S15), which is consistent with the COA, HOA and rBC particle types being predominantly externally mixed primary particles with little gas-to-particle condensation (or coagulation) of secondary particulate material prior to sampling (see Fig. 8).

3.7 Mixing of rBC-containing particles

Ternary diagrams that show the relative mass contributions of inorganic (nitrate and sulfate), organic and rBC in each particle class are used to evaluate the mixing states of rBC-containing particles in the sampled urban environment (see Fig. S16). According to Fig. S16 and Table 2, rBC is only a minor contributor to all particle types except the rBC class. The normalized number fraction of single particles, for each particle class, is shown in Fig. 10a as a function of the rBC mass fraction per single particle, demonstrating that only a small portion of particles from each class (except for the rBC class) is internally mixed with rBC (up to 60 wt %). Note that the total mass of each particle presented in Fig. 10a–c is calculated as the sum of organic, rBC, ammonium nitrate, and ammonium sulfate, assuming that all particles are completely neutralized (i.e., all nitrate and sulfate are in the form of ammonium salts; see Fig. S5c). Although the nitrate-rich class has an apparent relatively high rBC content compared to other classes, it is possibly due to the interference from the HCl$^+$ signal as discussed previously (Sect. 3.5 and Table 2).

Figure 10b and c further show the number distributions of particles categorized to the rBC and HOA classes, respectively, as a function of rBC mass fraction and particle d_{va}. Apparently, most of the HOA-rich particles contain very little (i.e., below detection limits) rBC mass as shown in the bar graph in Fig. 10c. A tail of the number distribution indicates that some small particles (~ 200 nm) are internally mixed with rBC by up to ~ 50 % by mass. On the other hand, Figure 10b suggests that rBC-rich particles are more gradually mixed with HOA materials with the average rBC mass fraction of ~ 0.7. Some nearly pure rBC particles are also observed in this study (i.e., mass fraction of rBC ~ 1). The number distributions of particles classified to other classes as a function of rBC mass fraction and particle d_{va} are shown in Fig. S17. The rBC content in the accumulation-mode particles is mainly associated with the secondary components,
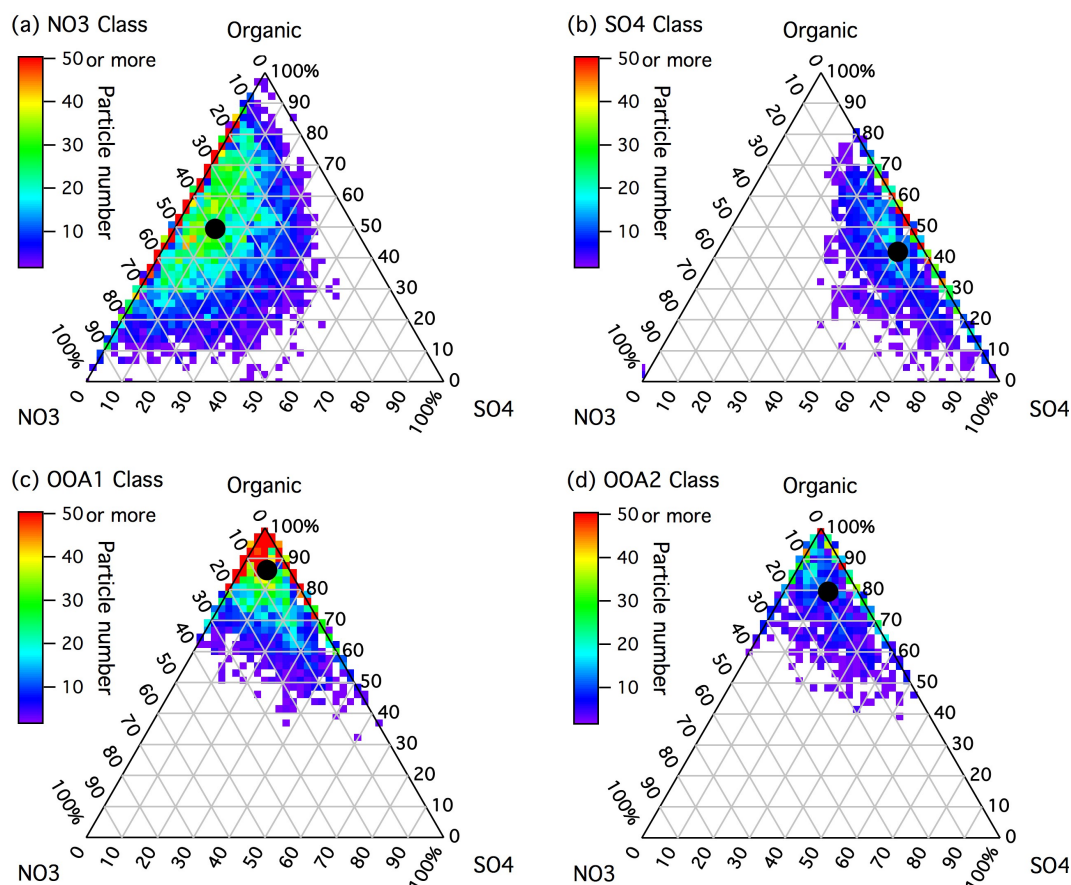
Figure 9. Ternary plot of nitrate, sulfate and organics mass fraction for those particles types identified by cluster analysis: **(a)** NO$_3$, **(b)** SO$_4$, **(c)** OOA1, and **(d)** OOA2. All these particle classes are the major contributors in the accumulation-mode particles. The black solid circles indicate the coordinates of average compositions of each particle classes.

indicating that those rBC-containing particles are chemically aged.

3.8   Low to mid-range d_{va} (~ 200–400 nm), organic-rich particles

The results provide a valuable, new perspective into the chemical composition and potential sources for low to mid-range d_{va} (~ 200–400 nm), organic-rich particles (i.e., dominated by particles in the HOA and COA clusters) using both ensemble and single particle techniques. Specifically, we made two sets of observations. (a) LS-SP-AMS ensemble data suggest that HOA and rBC were highly correlated in several ways: (1) time traces in Fig. 4a, (2) PToF size distributions in Fig. 2c, and (3) laser-on-to-laser-off ratios for PMF factors in Figs. S10 and S11. (b) LS-SP-AMS single particle results suggest that HOA- and COA-rich particles were nearly externally mixed with rBC. The strong correlation between HOA and rBC has, for the most part, been noted previously (Zhang et al., 2011, and references therein). The new observations obtained with the LS-SP-AMS single particle data and k-means cluster analysis suggest that the low

to mid-range d_{va}, organic-rich particles in a typical urban environment largely arise from low-density organic materials, such as nearly pure HOA and COA particles (> 95 wt % of organics) emitted from primary sources (e.g., vehicle exhaust and cooking emissions).

Even though the HOA-rich particles exhibit near external mixing with rBC, we note that HOA materials are nevertheless still more closely associated with rBC than are other particle constituents. As noted above, the laser-on-to-laser-off ratio increases by organic PMF factor in the following manner: HOA > OOA > COA (Fig. S11). This trend correlates well with the observed ensemble rBC mass fractions for each PMF factor. Hence, the difference between the PMF-HOA mass loadings from the laser-on and off modes suggests that HOA materials were more associated with rBC-containing particles than were OOA and COA. Furthermore, the HOA coating on rBC-rich particles alone is likely insufficient to explain the PMF-HOA difference between laser-on and off modes, at least for the current single particle size range. This suggests that some HOA-rich particles were likely associated with small rBC cores.
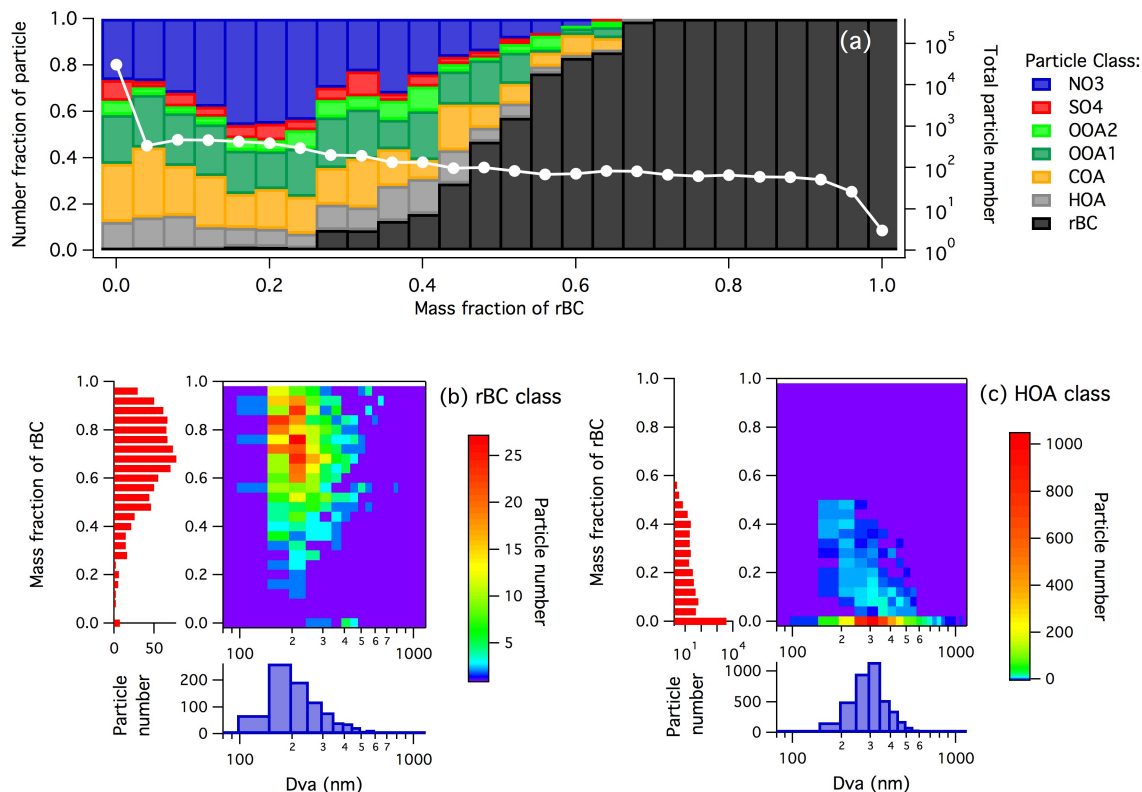
Figure 10. (a) Histogram (normalized to the total number of particles in each bin) of the mass fraction of rBC for all particle classes (left axis). The while circle markers represent the total number of particles (right axis) in each bin. Distributions of particle size and black carbon mass fraction for **(b)** rBC-rich class and **(c)** HOA-rich class.

Quantitatively, the single particle data analysis demonstrates that (1) a significant portion of HOA- and COA-rich particles ($> 90\%$) with particle d_{va} larger than ~ 200 nm did not contain a detectable amount of rBC, e.g., organic-rich particles containing a small rBC core or no rBC (with a mass contribution of rBC to the HOA- and COA-rich classes of about 3 % on average); and (2) the rBC-rich particles were mixed with ~ 28 wt % HOA-like material on average, e.g., a thinly HOA coated rBC particle, assuming uniform coating thickness. For example, applying a simple core-shell spherical structure (i.e., rBC core plus uniform HOA coating), a 200 nm d_{va} rBC-rich particle has a coating thickness of ~ 10 nm with HOA and rBC densities equal to 0.9 and 0.8 g cm^{-3}, respectively. rBC was mixed to a minor extent with other inorganic and organic materials. The total organic-to-rBC ratios are relatively constant across the size range of the rBC-rich cluster. However, whether this fact allows us to extend our mixing state conclusions to particles that are smaller than the nominal detection limit of the light scattering module is unknown.

The number fraction of rBC-containing particles to total prompt particles determined in the current study is about 7–11 % using m/z 36 as an rBC tracer and considering the potential interference from HCl^{+} (Table 2). Willis et al. (2014)

showed that the SP-AMS could measure rBC mass fractions down to at least 5 % by mass for laboratory-generated particle ensembles. The current data suggest that, per particle, rBC mass fractions for many of the HOA- and COA-rich single particles are less than 5 % (Table 2). We cannot rule out that the LS-SP-AMS is missing ion signals from small rBC cores in these particle types. The fact that the RIE$_{rBC}$ (usually from 0.2 to 0.4) is smaller than the RIE of other major NR-PM species indicates that we are getting fewer ion signals per mass from rBC compared to other NR-PM components, making it harder to determine if rBC is in any given particle. Using six ions as a detection limit of a single particle (i.e., a criteria for "prompt" particle type) and a mass-based ionization efficiency of Regal Black determined by calibration, it can be estimated that the detection limit of a pure rBC single particle is ~ 25 fg of rBC per particle. Therefore, the single particle mixing state measurements here may underrepresent the rBC-containing particle number (and mass) not only for low to mid-range d_{va}, organic-rich particles but also for all identified clusters.

3.9 Comparison of clustering observations with PMF factors

In addition to the mass spectral comparison provided in the previous section, Fig. 4 displays a comparison between the time series of organic classes (HOA, COA, and OOA classes, in ion signals) and PMF factors (in mass loadings). The total signals of the OOA classes shown in Fig. 4c were determined by the sum of organic signals from the nitrate, sulfate, OOA 1 and OOA 2 classes as they all contain oxygenated organic aerosol materials. The COA class completely captures the diurnal cycle of the PMF-COA (Fig. 4b), and the PMF-OOA agrees well with the OOA classes (Fig. 4c). The PMF-HOA factor exhibited three major peaks during the sampling period indicated by red dashed rectangles in Fig. 4a. However, the HOA class only captures the first two periods and not the last one. It is possible that most of the HOA material in this final period was associated with extremely small particles, which could not be detected by the light scattering module. The HOA-class organic signals displayed in Fig. 4a are not significantly altered by the addition of organic signals from the rBC class. Overall, the temporal variations of these organic particle classes and PMF factors correlate very well indicating that this single particle approach is able to largely capture the variability in the major aerosol components observed by LS-SP-AMS ensemble measurements.

4 Summary and concluding remarks

This work represents the first report of single particle characterization of rBC particles with the LS-SP-AMS. PMF analysis of ensemble data is a standard approach used to investigate the sources of ambient organic aerosol. Noting that the single particle data are direct measurements of aerosol composition whereas PMF analysis is a statistical tool, one of the major results from this paper is the temporal and compositional agreement between k-means single particle clusters and the PMF factors, which validate the PMF result and their relation to particulate matter sources. That being said, it is important to note that because the LS-SP-AMS may not be able to detect certain primary aerosol components, such as mineral dust, and non-IR absorbing refractory PM, the mixing state measurements obtained may not reflect the mixing state of the entire aerosol population.

Additional information regarding the mixing state of ambient particles and their size distributions (down to the detection limit of the light scattering module) is important for improving our understanding of the environmental impacts of atmospheric aerosol particles. While Liu et al. (2013) first applied the k-means clustering algorithm to LS-ToF-AMS data, this work successfully extends the application of the k-means clustering approach to analyze LS-SP-AMS data to evaluate the mixing state of ambient rBC particles and other non-refractory aerosol components. The approach presented here can be applied to assess the magnitude of the contributions of different sources when performing source–receptor analysis.

PMF analysis of ensemble measurements can provide information to evaluate the potential sources and aging of organic aerosol. While it is recognized that HOA factors, identified by PMF analysis of standard HR-ToF-AMS data, and rBC originate from combustion sources, the mixing states of these primary aerosol species cannot be easily characterized in this manner without the support of single particle measurements. Within the constraints of the instrumentation that may underrepresent the number of rBC-containing particles (see Sects. 3.3 and 3.8), the single particle data analysis demonstrates quantitatively that there were two types of particles associated with HOA materials: (1) HOA-rich particles associated with ∼ 3 wt % of rBC (e.g., a small rBC core with a high HOA content), and (2) rBC-rich particles mixed with ∼ 28 wt % of HOA-like material on average (e.g., a rBC particle with a thin, uniform HOA content). Other inorganic and organic materials were mixed to a lesser extent with rBC. The single particle data also provide insight into the sources of low to mid-range d_{va} organics (∼ 200–400 nm) in a typical urban environment. According to our cluster analysis, those organics are mainly composed of HOA- and COA-rich particles (with rBC content about 3 % on average) emitted from primary sources such as vehicle exhaust and kitchen emissions instead of processed particles associated with condensed secondary materials.

During our study, most of the rBC was likely freshly emitted from nearby vehicle exhaust and therefore we did not observe significant mixing, even though missing ion signals from small rBC cores in the aged particle types is possible. Further deployment of the LS-SP-AMS in remote environments will provide insight into the mixing state of aged ambient rBC. Freutel et al. (2013) recently developed a new particle categorization algorithm based on reference spectra comparison, which is potentially useful to identify unknown rBC particle types from LS-SP-AMS measurements.

The Supplement related to this article is available online at doi:10.5194/acp-15-1823-2015-supplement.

References

Allan, J. D., Williams, P. I., Morgan, W. T., Martin, C. L., Flynn, M. J., Lee, J., Nemitz, E., Phillips, G. J., Gallagher, M. W., and Coe, H.: Contributions from transport, solid fuel burning and cooking to primary organic aerosols in two UK cities, Atmos. Chem. Phys., 10, 647–668, doi:10.5194/acp-10-647-2010, 2010.

Allan, J., Delia, A., Coe, H., Bower, K., Alfarra, M., Jimenez, J., Middlebrook, A., Drewnick, F., Onasch, T., Canagaratna, M., Jayne, J., and Worsnop, D.: A generalised method for the extraction of chemically resolved mass spectra from Aerodyne aerosol mass spectrometer data, J. Aerosol Sci., 35, 909–922, 2004.

Baumgardner, D., Kok, G., and Raga, G.: Warming of the Arctic lower stratosphere by light absorbing particles, Geophys. Res. Lett., 31, L06117, 2004.

Bond, T. C., Doherty, S. J., Fahey, D. W., Forster, P. M., Berntsen, T., DeAngelo, B. J., Flanner, M. G., Ghan, S., Kaercher, B., Koch, D., Kinne, S., Kondo, Y., Quinn, P. K., Sarofim, M. C., Schultz, M. G., Schulz, M., Venkataraman, C., Zhang, H., Zhang, S., Bellouin, N., Guttikunda, S. K., Hopke, P. K., Jacobson, M. Z., Kaiser, J. W., Klimont, Z., Lohmann, U., Schwarz, J. P., Shindell, D., Storelvmo, T., Warren, S. G., and Zender, C. S.: Bounding the role of black carbon in the climate system: A scientific assessment, J.Geophys. Res.-Atmos., 118, 5380–5552, 2013.

Canagaratna, M. R., Jayne, J. T., Jimenez, J. L., Allan, J. D., Alfarra, M. R., Zhang, Q., Onasch, T. B., Drewnick, F., Coe, H., Middlebrook, A., Delia, A., Williams, L. R., Trimborn, A. M., Northway, M. J., DeCarlo, P. F., Kolb, C. E., Davidovits, P., and Worsnop, D. R.: Chemical and microphysical characterization of ambient aerosols with the aerodyne aerosol mass spectrometer, Mass Spectrom. Rev., 26, 185–222, 2007.

Canagaratna, M. R., Jayne, J. T., Ghertner, D. A., Herndon, S., Shi, Q., Jimenez, J. L., Silva, P. J., Williams, P., Lanni, T., Drewnick, F., Demerjian, K. L., Kolb, C. E., and Worsnop, D. R.: Chase studies of particulate emissions from in-use New York City vehicles, Aerosol Sci. Technol., 38, 555–573, 2004.

Cahill, J. F., Suski, K., Seinfeld, J. H., Zaveri, R. A., and Prather, K. A.: The mixing state of carbonaceous aerosol particles in northern and southern California measured during CARES and CalNex 2010, Atmos. Chem. Phys., 12, 10989–11002, doi:10.5194/acp-12-10989-2012, 2012.

Cappa, C. D., Onasch, T. B., Massoli, P., Worsnop, D. R., Bates, T. S., Cross, E. S., Davidovits, P., Hakala, J., Hayden, K. L., Jobson, B. T., Kolesar, K. R., Lack, D. A., Lerner, B. M., Li, S., Mellon, D., Nuaaman, I., Olfert, J. S., Petaja, T., Quinn, P. K., Song, C., Subramanian, R., Williams, E. J., and Zaveri, R. A.: Radiative Absorption Enhancements Due to the Mixing State of Atmospheric Black Carbon, Science, 337, 1078–1081, 2012.

China, S., Mazzoleni, C., Gorkowski, K., Aiken, A. C., and Dubey, M. K.: Morphology and mixing state of individual freshly emitted wildfire carbonaceous particles, Nat. Commun., 4, 2122, doi:10.1038/ncomms3122, 2013.

China, S., Salvadori, N., and Mazzoleni, C.: Effect of traffic and driving characteristics on morphology of atmospheric soot particles at freeway on-ramps, Environ. Sci. Technol., 48, 3128–3135, 2014.

Corbin, J. C., Sierau, B., Gysel, M., Laborde, M., Keller, A., Kim, J., Petzold, A., Onasch, T. B., Lohmann, U., and Mensah, A. A.: Mass spectrometry of refractory black carbon particles from

six sources: carbon-cluster and oxygenated ions, Atmos. Chem. Phys., 14, 2591–2603, doi:10.5194/acp-14-2591-2014, 2014.

Cross, E. S., Slowik, J. G., Davidovits, P., Allan, J. D., Worsnop, D. R., Jayne, J. T., Lewis, D. K., Canagaratna, M., and Onasch, T. B.: Laboratory and ambient particle density determinations using light scattering in conjunction with aerosol mass spectrometry, Aerosol Sci. Technol., 41, 343–359, 2007.

Cross, E. S., Onasch, T. B., Canagaratna, M., Jayne, J. T., Kimmel, J., Yu, X.-Y., Alexander, M. L., Worsnop, D. R., and Davidovits, P.: Single particle characterization using a light scattering module coupled to a time-of-flight aerosol mass spectrometer, Atmos. Chem. Phys., 9, 7769–7793, doi:10.5194/acp-9-7769-2009, 2009.

Cross, E. S., Onasch, T. B., Ahern, A., Wrobel, W., Slowik, J. G., Olfert, J., Lack, D. A., Massoli, P., Cappa, C. D., Schwarz, J. P., Spackman, J. R., Fahey, D. W., Sedlacek, A., Trimborn, A., Jayne, J. T., Freedman, A., Williams, L. R., Ng, N. L., Mazzoleni, C., Dubey, M., Brem, B., Kok, G., Subramanian, R., Freitag, S., Clarke, A., Thornhill, D., Marr, L. C., Kolb, C. E., Worsnop, D. R., and Davidovits, P.: Soot Particle StudiesInstrument Inter-ComparisonProject Overview, Aerosol Sci. Technol., 44, 592–611, 2010.

Dallmann, T. R., Onasch, T. B., Kirchstetter, T. W., Worton, D. R., Fortner, E. C., Herndon, S. C., Wood, E. C., Franklin, J. P., Worsnop, D. R., Goldstein, A. H., and Harley, R. A.: Characterization of particulate matter emissions from on-road gasoline and diesel vehicles using a soot particle aerosol mass spectrometer, Atmos. Chem. Phys., 14, 7585–7599, doi:10.5194/acp-14-7585-2014, 2014.

DeCarlo, P. F., Slowik, J. G., Worsnop, D. R., Davidovits, P., and Jimenez, J. L.: Particle morphology and density characterization by combined mobility and aerodynamic diameter measurements. Part 1: Theory, Aerosol Sci. Technol., 38, 1185–1205, 2004.

DeCarlo, P. F., Kimmel, J. R., Trimborn, A., Northway, M. J., Jayne, J. T., Aiken, A. C., Gonin, M., Fuhrer, K., Horvath, T., Docherty, K. S., Worsnop, D. R., and Jimene, J. L.: Field-deployable, high-resolution, time-of-flight aerosol mass spectrometer, Anal. Chem., 78, 8281–8289, 2006.

Drewnick, F., Hings, S. S., DeCarlo, P. F., Jayne, J. T., Gonin, M., Fuhrer, K., Weimer, S., Jimenez, J. L., Demerjian, K. L., Borrmann, S., and Worsnop, D. R.: A new time-of-flight aerosol mass spectrometer (TOF-AMS) - Instrument description and first field deployment, Aerosol Sci. Technol., 39, 637–658, 2005.

Docherty, K. S., Jaoui, M., Corse, E., Jimenez, J. L., Offenberg, J. H., Lewandowski, M., and Kleindienst, T. E.: Collection Efficiency of the Aerosol Mass Spectrometer for Chamber-Generated Secondary Organic Aerosols, Aerosol Sci. Technol., 47, 294–309, 2013.

Freutel, F., Drewnick, F., Schneider, J., Klimach, T., and Borrmann, S.: Quantitative single-particle analysis with the Aerodyne aerosol mass spectrometer: development of a new classification algorithm and its application to field data, Atmos. Meas. Tech., 6, 3131–3145, doi:10.5194/amt-6-3131-2013, 2013.

Friedman, B., Herich, H., Kammermann, L., Gross, D. S., Arneth, A., Holst, T., and Cziczo, D. J.: Subarctic atmospheric aerosol composition: 1. Ambient aerosol characterization, J.Geophys. Res.-Atmos., 114, D13203, doi:10.1029/2009JD011772, 2009.

Giorio, C., Tapparo, A., Dall'Osto, M., Harrison, R. M., Beddows, D. C. S., Di Marco, C., and Nemitz, E.: Comparison of three

techniques for analysis of data from an Aerosol Time-of-Flight Mass Spectrometer, Atmos. Environ., 61, 316–326, 2012.

Gross, D. S., Atlas, R., Rzeszotarski, J., Turetsky, E., Christensen, J., Benzaid, S., Olson, J., Smith, T., Steinberg, L., Sulman, J., Ritz, A., Anderson, B., Nelson, C., Musicant, D. R., Chen, L., Snyder, D. C., and Schauer, J. J.: Environmental chemistry through intelligent atmospheric data analysis, Environ. Modell. Softw., 25, 760–769, 2010.

Healy, R. M., Hellebust, S., Kourtchev, I., Allanic, A., O'Connor, I. P., Bell, J. M., Healy, D. A., Sodeau, J. R., and Wenger, J. C.: Source apportionment of PM$_{2.5}$ in Cork Harbour, Ireland using a combination of single particle mass spectrometry and quantitative semi-continuous measurements, Atmos. Chem. Phys., 10, 9593–9613, doi:10.5194/acp-10-9593-2010, 2010.

Healy, R. M., Sciare, J., Poulain, L., Crippa, M., Wiedensohler, A., Prévôt, A. S. H., Baltensperger, U., Sarda-Estève, R., McGuire, M. L., Jeong, C.-H., McGillicuddy, E., O'Connor, I. P., Sodeau, J. R., Evans, G. J., and Wenger, J. C.: Quantitative determination of carbonaceous particle mixing state in Paris using single-particle mass spectrometer and aerosol mass spectrometer measurements, Atmos. Chem. Phys., 13, 9479–9496, doi:10.5194/acp-13-9479-2013, 2013.

Jacobson, M.: Strong radiative heating due to the mixing state of black carbon in atmospheric aerosols, Nature, 409, 695–697, 2001.

Jayne, J.T., Leard, D.C., Zhang, X., Davidovits, P., Smith, K.A., Kolb, C.E., and Worsnop, D.R.: Development of an Aerosol Mass Spectrometer for Size and Composition. Analysis of Submicron Particles, Aerosol Sci. Technol., 33, 49–70, 2000.

Jimenez, J. L., Jayne, J. T., Shi, Q., Kolb, C. E., Worsnop, D. R., Yourshaw, I., Seinfeld, J. H., Flagan, R. C., Zhang, X., Smith, K. A., Morris, J. W., and Davidovits, P.: Ambient aerosol sampling using the Aerodyne Aerosol Mass Spectrometer, J.Geophys. Res.-Atmos, 108, 8425, doi:10.1029/2001JD001213, 2003.

Jimenez, J. L., Canagaratna, M. R., Donahue, N. M., Prevot, A. S. H., Zhang, Q., Kroll, J. H., DeCarlo, P. F., Allan, J. D., Coe, H., Ng, N. L., Aiken, A. C., Docherty, K. S., Ulbrich, I. M., Grieshop, A. P., Robinson, A. L., Duplissy, J., Smith, J. D., Wilson, K. R., Lanz, V. A., Hueglin, C., Sun, Y. L., Tian, J., Laaksonen, A., Raatikainen, T., Rautiainen, J., Vaattovaara, P., Ehn, M., Kulmala, M., Tomlinson, J. M., Collins, D. R., Cubison, M. J., Dunlea, E. J., Huffman, J. A., Onasch, T. B., Alfarra, M. R., Williams, P. I., Bower, K., Kondo, Y., Schneider, J., Drewnick, F., Borrmann, S., Weimer, S., Demerjian, K., Salcedo, D., Cottrell, L., Griffin, R., Takami, A., Miyoshi, T., Hatakeyama, S., Shimono, A., Sun, J. Y., Zhang, Y. M., Dzepina, K., Kimmel, J. R., Sueper, D., Jayne, J. T., Herndon, S. C., Trimborn, A. M., Williams, L. R., Wood, E. C., Middlebrook, A. M., Kolb, C. E., Baltensperger, U., and Worsnop, D. R.: Evolution of Organic Aerosols in the Atmosphere, Science, 326, 1525–1529, 2009.

Lack, D. A., Langridge, J. M., Bahreini, R., Cappa, C. D., Middlebrook, A. M., and Schwarz, J. P.: Brown carbon and internal mixing in biomass burning particles, Proc. Natl. Acad. Sci. USA, 109, 14802–14807, 2012.

Lanz, V. A., Alfarra, M. R., Baltensperger, U., Buchmann, B., Hueglin, C., and Prévôt, A. S. H.: Source apportionment of submicron organic aerosols at an urban site by factor analytical modelling of aerosol mass spectra, Atmos. Chem. Phys., 7, 1503–1522, doi:10.5194/acp-7-1503-2007, 2007.

Liu, S., Russell, L. M., Sueper, D. T., and Onasch, T. B.: Organic particle types by single-particle measurements using a time-of-flight aerosol mass spectrometer coupled with a light scattering module, Atmos. Meas. Tech., 6, 187–197, doi:10.5194/amt-6-187-2013, 2013.

Massoli, P., Fortner, E. C., Canagaratna, M. R., Williams, L. R., Zhang, Q., Sun, Y., Schwab, J. J., Trimborn, A., Onasch, T. B., Demerjian, K. L., Kolb, C. E., Worsnop, D. R., and Jayne, J. T.: Pollution Gradients and Chemical Characterization of Particulate Matter from Vehicular Traffic near Major Roadways: Results from the 2009 Queens College Air Quality Study in NYC, Aerosol Sci. Technol., 46, 1201–1218, 2012.

Matthew, B. M., Middlebrook, A. M., and Onasch, T. B.: Collection efficiencies in an Aerodyne Aerosol Mass Spectrometer as a function of particle phase for laboratory generated aerosols, Aerosol Sci. Technol., 42, 884–898, 2008.

McMeeking, G. R., Good, N., Petters, M. D., McFiggans, G., and Coe, H.: Influences on the fraction of hydrophobic and hydrophilic black carbon in the atmosphere, Atmos. Chem. Phys., 11, 5099–5112, doi:10.5194/acp-11-5099-2011, 2011.

Metcalf, A. R., Loza, C. L., Coggon, M. M., Craven, J. S., Jonsson, H. H., Flagan, R. C., and Seinfeld, J. H.: Secondary Organic Aerosol Coating Formation and Evaporation: Chamber Studies Using Black Carbon Seed Aerosol and the Single-Particle Soot Photometer, Aerosol Sci. Technol., 47, 326–347, 2013.

Middlebrook, A. M., Bahreini, R., Jimenez, J. L., and Canagaratna, M. R.: Evaluation of composition-dependent collection efficiencies for the Aerodyne aerosol mass spectrometer using field data, Aerosol. Sci. Technol., 46, 258–271, 2012.

Moffet, R. C., and Prather, K. A.: In-situ measurements of the mixing state and optical properties of soot with implications for radiative forcing estimates, Proc. Natl. Acad. Sci., 106, 11872–11877, 2009.

Mohr, C., Huffman, J. A., Cubison, M. J., Aiken, A. C., Docherty, K. S., Kimmel, J. R., Ulbrich, I. M., Hannigan, M., and Jimenez, J. L.: Characterization of Primary Organic Aerosol Emissions from Meat Cooking, Trash Burning, and Motor Vehicles with High-Resolution Aerosol Mass Spectrometry and Comparison with Ambient and Chamber Observations, Environ. Sci. Technol., 43, 2443–2449, 2009.

Mohr, C., DeCarlo, P. F., Heringa, M. F., Chirico, R., Slowik, J. G., Richter, R., Reche, C., Alastuey, A., Querol, X., Seco, R., Peñuelas, J., Jiménez, J. L., Crippa, M., Zimmermann, R., Baltensperger, U., and Prévôt, A. S. H.: Identification and quantification of organic aerosol from cooking and other sources in Barcelona using aerosol mass spectrometer data, Atmos. Chem. Phys., 12, 1649–1665, doi:10.5194/acp-12-1649-2012, 2012.

Moteki, N. and Kondo, Y.: Effects of mixing state on black carbon measurements by laser-induced incandescence, Aerosol Sci. Technol., 41, 398–417, 2007.

Ng, N. L., Canagaratna, M. R., Zhang, Q., Jimenez, J. L., Tian, J., Ulbrich, I. M., Kroll, J. H., Docherty, K. S., Chhabra, P. S., Bahreini, R., Murphy, S. M., Seinfeld, J. H., Hildebrandt, L., Donahue, N. M., DeCarlo, P. F., Lanz, V. A., Prévôt, A. S. H., Dinar, E., Rudich, Y., and Worsnop, D. R.: Organic aerosol components observed in Northern Hemispheric datasets from Aerosol Mass Spectrometry, Atmos. Chem. Phys., 10, 4625–4641, doi:10.5194/acp-10-4625-2010, 2010.

Onasch, T. B., Trimborn, A., Fortner, E. C., Jayne, J. T., Kok, G. L., Williams, L. R., Davidovits, P., and Worsnop, D. R.: Soot Particle Aerosol Mass Spectrometer: Development, Validation, and Initial Application, Aerosol Sci. Technol., 46, 804–817, 2012.

Pagels, J., Dutcher, D. D., Stolzenburg, M. R., McMurry, P. H., Gaelli, M. E., and Gross, D. S.: Fine-particle emissions from solid biofuel combustion studied with single-particle mass spectrometry: Identification of markers for organics, soot, and ash components, J.Geophys. Res.-Atmos., 118, 859–870, 2013.

Pratt, K. A. and Prather, K. A.: Mass spectrometry of atmospheric aerosols: Recent developments and applications. Part II: On-line mass spectrometry techniques, Mass Spectrom. Rev., 31, 17–48, 2012.

Rebotier, T. P. and Prather, K. A.: Aerosol time-of-flight mass spectrometry data analysis: a benchmark of clustering algorithms, Anal. Chim. Acta, 585, 38–54, doi:10.1016/j.aca.2006.12.009, 2007.

Robinson, E. S., Saleh, R., and Donahue, N. M.: Organic aerosol mixing observed by single-particle mass spectrometry., J. Phys. Chem. A, 117, 13935–13945, doi:10.1021/jp405789t, 2013.

Schwarz, J. P., Gao, R. S., Fahey, D. W., Thomson, D. S., Watts, L. A., Wilson, J. C., Reeves, J. M., Darbeheshti, M., Baumgardner, D. G., Kok, G. L., Chung, S. H., Schulz, M., Hendricks, J., Lauer, A., Kaercher, B., Slowik, J. G., Rosenlof, K. H., Thompson, T. L., Langford, A. O., Loewenstein, M., and Aikin, K. C.: Single-particle measurements of midlatitude black carbon and light-scattering aerosols from the boundary layer to the lower stratosphere, J. Geophys. Res.-Atmos., 111, D16207, doi:10.1029/2006JD007076, 2006.

Shields, L. G., Suess, D. T., and Prather, K. A.: Determination of single particle mass spectral signatures from heavy-duty diesel vehicle emissions for PM2.5 source apportionment, Atmos. Environ., 41, 3841–3852, 2007.

Shields, L. G., Qin, X. Y., Toner, S. M., and Prather, K. A.: Detection of ambient ultrafine aerosols by single particle techniques during the SOAR 2005 campaign, Aerosol Sci. Technol., 42, 674–684, doi:10.1080/02786820802227378, 2008.

Shiraiwa, M., Kondo, Y., Moteki, N., Takegawa, N., Miyazaki, Y., and Blake, D. R.: Evolution of mixing state of black carbon in polluted air from Tokyo, Geophys. Res. Lett., 34, L16803, doi:10.1029/2007GL029819, 2007.

Shiraiwa, M., Kondo, Y., Iwamoto, T., and Kita, K.: Amplification of Light Absorption of Black Carbon by Organic Coating, Aerosol Sci. Technol., 44, 46–54, 2010.

Slowik, J., Stainken, K., Davidovits, P., Williams, L., Jayne, J., Kolb, C., Worsnop, D., Rudich, Y., DeCarlo, P., and Jimenez, J.: Particle morphology and density characterization by combined mobility and aerodynamic diameter measurements. Part 2: Application to combustion-generated soot aerosols as a function of fuel equivalence ratio, Aerosol Sci. Technol., 38, 1206–1222, 2004.

Sodeman, D. A., Toner, S. M., and Prather, K. A.: Determination of single particle mass spectral signatures from light-duty vehicle emissions, Environ. Sci. Technol., 39, 4569–4580, 2005.

Stephens, M., Turner, N., and Sandberg, J.: Particle identification by laser-induced incandescence in a solid-state laser cavity, Appl. Opt., 42, 3726–3736, 2003.

Toner, S. M., Sodeman, D. A., and Prather, K. A.: Single particle characterization of ultrafine and accumulation mode particles from heavy duty diesel vehicles using aerosol time-of-flight mass spectrometry, Environ. Sci. Technol., 40, 3912–3921, 2006.

Toner, S. M., Shields, L. G., Sodeman, D. A., and Prather, K. A.: Using mass spectral source signatures to apportion exhaust particles from gasoline and diesel powered vehicles in a freeway study using UF-ATOFMS, Atmos. Environ., 42, 568–581, 2008.

Tritscher, T., Juranyi, Z., Martin, M., Chirico, R., Gysel, M., Heringa, M. F., DeCarlo, P. F., Sierau, B., Prevot, A. S. H., Weingartner, E., and Baltensperger, U.: Changes of hygroscopicity and morphology during ageing of diesel soot, Environ. Res. Lett., 6, 034026, doi:10.1088/1748-9326/6/3/034026, 2011.

Ulbrich, I. M., Canagaratna, M. R., Zhang, Q., Worsnop, D. R., and Jimenez, J. L.: Interpretation of organic components from Positive Matrix Factorization of aerosol mass spectrometric data, Atmos. Chem. Phys., 9, 2891–2918, doi:10.5194/acp-9-2891-2009, 2009.

Wang, J., Cubison, M. J., Aiken, A. C., Jimenez, J. L., and Collins, D. R.: The importance of aerosol mixing state and size-resolved composition on CCN concentration and the variation of the importance with atmospheric aging of aerosols, Atmos. Chem. Phys., 10, 7267–7283, doi:10.5194/acp-10-7267-2010, 2010.

Willis, M. D., Lee, A. K. Y., Onasch, T. B., Fortner, E. C., Williams, L. R., Lambe, A. T., Worsnop, D. R., and Abbatt, J. P. D.: Collection efficiency of the soot-particle aerosol mass spectrometer (SP-AMS) for internally mixed particulate black carbon, Atmos. Meas. Tech., 7, 4507–4516, doi:10.5194/amt-7-4507-2014, 2014.

Zhang, Q., Jimenez, J. L., Canagaratna, M. R., Allan, J. D., Coe, H., Ulbrich, I., Alfarra, M. R., Takami, A., Middlebrook, A. M., Sun, Y. L., Dzepina, K., Dunlea, E., Docherty, K., DeCarlo, P. F., Salcedo, D., Onasch, T., Jayne, J. T., Miyoshi, T., Shimono, A., Hatakeyama, S., Takegawa, N., Kondo, Y., Schneider, J., Drewnick, F., Borrmann, S., Weimer, S., Demerjian, K., Williams, P., Bower, K., Bahreini, R., Cottrell, L., Griffin, R. J., Rautiainen, J., Sun, J. Y., Zhang, Y. M., and Worsnop, D. R.: Ubiquity and dominance of oxygenated species in organic aerosols in anthropogenically-influenced Northern Hemisphere midlatitudes, Geophys. Res. Lett., 34, L13801, doi:10.1029/2007GL029979, 2007.

Zhang, Q., Jimenez, J. L., Canagaratna, M. R., Ulbrich, I. M., Ng, N. L., Worsnop, D. R., and Sun, Y.: Understanding atmospheric organic aerosols via factor analysis of aerosol mass spectrometry: a review, Analyt. Bioanalyt. Chem., 401, 3045–3067, 2011.

Zhang, R., Khalizov, A. F., Pagels, J., Zhang, D., Xue, H., and McMurry, P. H.: Variability in morphology, hygroscopicity, and optical properties of soot aerosols during atmospheric processing, Proc. Natl. Acad. Sci. USA, 105, 10291–10296, 2008.